JGR Space Physics

RESEARCH ARTICLE
10.1029/2026JA035251

Calculating Quasi-Linear Diffusion Rates Using Different Methods to Specify the Wave Spectrum

J. D. Sadler[1,2], **R. B. Horne**[1], **S. A. Glauert**[1], **T. A. Daggitt**[1], **J. M. Albert**[3], and **G. Del Zanna**[2,4]

[1]British Antarctic Survey, Cambridge, UK, [2]Department of Applied Mathematics and Theoretical Physics, University of Cambridge, Cambridge, UK, [3]Air Force Research Laboratory, Kirtland Air Force Base, Albuquerque, NM, USA, [4]School of Physics and Astronomy, University of Leicester, Leicester, UK

Key Points:

- We calculate quasi-linear diffusion rates using three different methods to specify the wave spectrum
- We use input parameters typical of electromagnetic waves observed in the inner magnetosphere
- Differences between the methods and existing diffusion rates used in the BAS Radiation Belt Model are very small

Correspondence to:

J. D. Sadler,
jodler77@bas.ac.uk

Citation:

Sadler, J. D., Horne, R. B., Glauert, S. A., Daggitt, T. A., Albert, J. M., & Del Zanna, G. (2026). Calculating quasi-linear diffusion rates using different methods to specify the wave spectrum. *Journal of Geophysical Research: Space Physics*, *131*, e2026JA035251. https://doi.org/10.1029/2026JA035251

Received 19 FEB 2026
Accepted 2 APR 2026

Author Contributions:

Conceptualization: J. D. Sadler, R. B. Horne, S. A. Glauert, T. A. Daggitt, J. M. Albert, G. Del Zanna
Formal analysis: J. D. Sadler
Methodology: J. D. Sadler, R. B. Horne, S. A. Glauert, T. A. Daggitt, J. M. Albert, G. Del Zanna
Software: J. D. Sadler, S. A. Glauert, T. A. Daggitt
Supervision: R. B. Horne, S. A. Glauert, G. Del Zanna
Visualization: J. D. Sadler
Writing – original draft: J. D. Sadler
Writing – review & editing: R. B. Horne, S. A. Glauert, T. A. Daggitt, J. M. Albert, G. Del Zanna

Abstract Quasi-linear diffusion theory is widely used in radiation belt modeling to describe resonant interactions between charged particles and electromagnetic waves. The diffusion rates depend on the wave spectrum and properties of the background plasma. For decades many studies have used variations of a longstanding method to specify the wave spectrum. Recently, a new method was proposed, and it was suggested the resulting diffusion rates can differ by orders of magnitude. Large differences in the diffusion rates would cause significant changes in the relativistic electron flux predicted by radiation belt models. We calculate quasi-linear diffusion rates using three methods to specify the wave spectrum: two variations of the longstanding method and the new method. All three methods have the same wave power at each frequency, but the weighting of wave energy with respect to wave normal angle is different. We use input parameters typical of wave observations in the inner magnetosphere, including lower band and upper band chorus, hiss waves, electromagnetic ion cyclotron waves and fast magnetosonic waves. We find very small differences between the new method and the method used to calculate diffusion rates for the British Antarctic Survey Radiation Belt Model. We conclude that the uncertainties in modeling global variations in the radiation belts are more likely due to statistical sampling of wave data, rather than the method of calculating diffusion rates.

Plain Language Summary Charged particles in near-Earth space interact with naturally occurring electromagnetic waves. These interactions can accelerate electrons to high energies or scatter them into Earth's atmosphere. Understanding these processes is important because energetic electrons pose a risk to satellite infrastructure. Many simulations model the electron population using a diffusion equation, where the amount of electron acceleration and scattering is related to the diffusion rates. The diffusion rates depend on several inputs, including the frequency and angular spread of the waves. For decades many studies have calculated diffusion rates using variations of a longstanding method to specify the frequency and angular spread of the waves. Recently, a new method was proposed, and it was suggested that the results can differ significantly in some situations. In this study we compare three different methods to specify the frequency and angular spread of the waves in diffusion rate calculations. We use realistic input parameters that are typical of observed wave types. We find very small differences between the new method and the existing method used for the British Antarctic Survey Radiation Belt Model. We conclude that uncertainties in the diffusion rates are more likely due to statistical sampling of wave data, rather than the method of calculation.

1. Introduction

Charged particles in the inner magnetosphere interact with a variety of electromagnetic waves (Thorne, 2010). The waves drive acceleration and loss processes that change the flux of relativistic electrons in Earth's radiation belts by orders of magnitude during geomagnetic storms (Baker et al., 1994; Li & Hudson, 2019). Understanding the variability of the radiation belts is important because energetic electrons damage satellite infrastructure (Baker et al., 2017; Iucci et al., 2005; Wrenn, 1995).

Global radiation belt models typically use quasi-linear theory to describe electron pitch angle and energy diffusion due to wave-particle interactions. Quasi-linear theory describes diffusion of the particle distribution function under the influence of a specified wave spectrum (Kennel & Engelmann, 1966; Lerche, 1968). The diffusion rates depend on the wave spectrum and properties of the background plasma, which vary with spatial location and geomagnetic activity. To facilitate accurate diffusion rate calculations, global surveys combining data from multiple satellites have been used to construct statistical models of wave activity as a function of magnetic latitude, magnetic local time (MLT), L^* and geomagnetic activity (e.g., Meredith et al., 2018). Although quasi-linear theory was originally developed for local diffusion rates in a homogeneous plasma, variations along a geomagnetic field line are included by calculating a local diffusion rate at each magnetic latitude and averaging over an unperturbed particle bounce trajectory (Lyons et al., 1972). These bounce-averaged diffusion rates depend on MLT, L^* and geomagnetic activity, as well as the equatorial pitch-angle and kinetic energy of the particle.

Many dynamic global radiation belt models rely on quasi-linear diffusion rates. A few, such as VERB-4D (Shprits et al., 2015) and RAM-SCB (Jordanova et al., 2023) include MLT resolution and use MLT-dependent bounce-averaged diffusion rates. However, most radiation belt models are drift-averaged and use diffusion rates which are averaged over MLT. Such models include Salammbo (Varotsou et al., 2005), VERB (Subbotin & Shprits, 2009), Albert et al. (2009), DREAM3D (Tu et al., 2014) and the British Antarctic Survey Radiation Belt Model (BAS-RBM) (Glauert et al., 2014). The models include numerous wave types, for example, the BAS-RBM includes lower and upper band chorus waves, hiss waves, fast magnetosonic waves, electromagnetic ion cyclotron (EMIC) waves, lightning-generated whistlers and anthropogenic VLF transmitter waves. The diffusion rates characterize the effect of each wave type, so they are crucial to understanding radiation belt dynamics. The BAS-RBM also provides forecasts of the outer radiation belt for the satellite risk prediction and radiation forecast (SaRIF) system (Horne et al., 2021), so the diffusion rates ultimately contribute to space weather prediction and help ensure the safe operation of satellites.

Quasi-linear theory is applicable to any linear plasma wave mode propagating at arbitrary angles to the background magnetic field, and the diffusion rates depend on the magnetic power spectral density in wavevector space (see Section 2). Lyons (1974) calculated quasi-linear diffusion rates due to resonant interactions with whistler and EMIC waves using a high-density approximation for the cold plasma dispersion relation, and specified the magnetic power spectral density using a method first introduced by Lyons et al. (1971). Glauert and Horne (2005) and Albert (2005) used the full cold plasma dispersion relation for a relativistic magnetized plasma of arbitrary density, and the same method as the earlier papers to specify the power spectral density. The results showed that acceleration by whistler-mode chorus waves can explain the observed increase in MeV electron fluxes in the outer radiation belt (Horne, Thorne, Glauert, et al., 2005; Horne, Thorne, Shprits, et al., 2005). The methods of Glauert and Horne (2005) and Albert (2005) have since been widely used to calculate diffusion rates for radiation belt modeling, including all the models referenced earlier in this section. Thus, the expressions for the magnetic power spectral density introduced by Lyons et al. (1971) continue to be used in radiation belt physics more than half a century later.

Cunningham (2023) proposed a new method to specify the magnetic power spectral density, which has conceptual and practical advantages. Cunningham showed that the new method produces diffusion rates which differ from the traditional method by several orders of magnitude when waves propagate very near to the cold plasma resonance cone, suggesting that previous work should be reviewed. Large differences in the diffusion rates would cause significant changes in the relativistic electron flux predicted by radiation belt models. However, many previous studies have used modifications of the traditional method that mitigate known issues at the resonance cone. For example, diffusion rates used in the BAS-RBM have been calculated by suppressing the magnetic wave power at the resonance cone (Horne et al., 2013). In this study we calculate quasi-linear diffusion rates using three methods to specify the wave spectrum: the original method of Glauert and Horne (2005), the modification of Horne et al. (2013) and the new method of Cunningham (2023). We use input parameters typical of waves observed in the inner magnetosphere, including lower and upper band chorus waves, hiss waves, EMIC waves and fast magnetosonic waves. We find very small differences between Cunningham's approach and the method used to calculate existing diffusion rates for the BAS-RBM. The results are explained by considering the distribution of wave energy with respect to wave normal angle in each method.

2. Methodology

2.1. Three Methods to Specify the Wave Spectrum

The local pitch angle diffusion rate is given by

$$D_{\alpha\alpha} = \sum_{n=n_l}^{n=n_h} \int_{X_{\min}}^{X_{\max}} X D_{\alpha\alpha}^{nX} dX, \tag{1}$$

where n is the integer harmonic, $X = \tan\theta$ is the tangent of the wave normal angle and the waves are restricted to propagate between $X_{\min}$ and $X_{\max}$. The subscripts $\alpha\alpha$ can be replaced by EE and αE to obtain the energy and mixed pitch angle-energy diffusion rates. The lengthy expressions for $D_{\alpha\alpha}^{nX}$, D_{EE}^{nX} and $D_{\alpha E}^{nX}$ are described in detail elsewhere (e.g., Glauert & Horne, 2005) so they are omitted here, but it is important to note that $D_{\alpha\alpha}^{n,X} \propto |\vec{B}_k(\vec{k})|^2/V$ (and similarly for D_{EE}^{nX} and $D_{\alpha E}^{nX}$). Here $\vec{B}_k$ is the spatial Fourier transform of the wave magnetic field and V is a plasma volume. The quantity $|\vec{B}_k|^2/V$ is the magnetic power spectral density in Cartesian wavevector space (k_x, k_y, k_z) such that

$$\int \frac{1}{(2\pi)^3} \frac{|B_k|^2}{V} d^3\vec{k} = B_{wave}^2, \tag{2}$$

and B_{wave}^2 is the average squared wave magnetic field over space and time. Therefore, $|\vec{B}_k|^2/V$ is analogous to the power spectral density $B^2(\omega)$ in frequency space which satisfies

$$\int_0^\infty B^2(\omega) d\omega = B_{wave}^2. \tag{3}$$

The magnetic power spectral density is closely related to the wave distribution function introduced by Storey and Lefeuvre (1979), which also specifies the distribution of wave energy in wavevector space. Whilst Storey and Lefeuvre consider the ensemble average of a random electromagnetic wave field, the $|B_k|^2/V$ factor in the diffusion rates arises from the Fourier transform of the wave electric and magnetic fields, which are related by Faraday's law (Lyons, 1974).

Calculating $\vec{B}_k$ directly would require measuring the wave magnetic field throughout the spatial domain, which is not possible with a single spacecraft. In fact, instruments often only provide $B^2(\omega)$ in frequency space. Therefore, Lyons et al. (1971) and Lyons (1974) related the distributions in wavevector space and frequency space using

$$\frac{|\vec{B}_k|^2}{V} = \frac{B^2(\omega) g(\omega, X)}{N(\omega)} = \frac{B^2(\omega) g(\omega, X)}{\frac{1}{2\pi^2} \int_{X_{\min}}^{X_{\max}} g(\omega, X) \frac{k^2 X}{(1+X^2)^{3/2}} \left. \frac{\partial k}{\partial \omega} \right|_X dX}, \tag{4}$$

where $g(\omega, X)$ determines the distribution of wave power over wave normal angle at a given frequency. The normalization function $N(\omega)$ was introduced to ensure that the wave power per unit frequency is $B^2(\omega)$ in line with Equation 3. Lyons (1974) used $g(\omega, X) = \exp(-X^2/X_w^2)$ (independent of ω) to specify a wave spectrum peaked in the field-aligned direction and calculate diffusion rates.

Many subsequent studies, including Glauert and Horne (2005) and Albert (2005), followed Lyons in using Equation 4 to model the wave spectrum. Issues can arise, however, when waves propagate near the resonance cone angle θ_{rc}, where $X_{rc}(\omega) = \tan(\theta_{rc}) = \sqrt{-P/S}$ and P and S are the conventional Stix parameters for a cold plasma. On the whistler branch, no solution to the cold plasma dispersion relation exists for $\theta > \theta_{rc}$, so we must take $X_{\max} \leq X_{rc}(\omega)$. However, if $g(\omega, X_{rc}(\omega)) > 0$ and $X_{\max} = X_{rc}(\omega)$, $N(\omega)$ cannot be evaluated because the expression is not integrable. This is because as $X \to X_{rc}(\omega)$ the refractive index $\mu = ck/\omega$ scales as $\left(X_{rc}^2(\omega) - X^2\right)^{-1/2}$ and thus the term $\frac{k^2 X}{(1+X^2)^{3/2}} \left.\frac{\partial k}{\partial \omega}\right|_X$ scales as $\left(X_{rc}^2(\omega) - X^2\right)^{-5/2}$, which is not integrable if $X_{\max} = X_{rc}(\omega)$ (Cunningham, 2023).

If $X_{\max} < X_{rc}(\omega)$ then $N(\omega)$ can be calculated. Glauert and Horne (2005) chose to set $X_{\max} = \min\left(X_{\max}^{in}, (1-\epsilon) X_{rc}(\omega)\right)$, where $X_{\max}^{in}$ is the upper limit specified by the user and $\epsilon = 10^{-4}$. However, $N(\omega)$ can become arbitrarily large as $\epsilon \to 0$, and the resulting diffusion rates are very sensitive to the choice of ϵ.

Alternatively, $X_{\max}$ can be chosen corresponding to a maximum refractive index $\mu_{\max}$. The maximum refractive index observed by satellites is controlled by hot plasma effects, primarily wave dispersion modifications by suprathermal electrons, but also by Landau damping (Artemyev et al., 2016; Ma et al., 2017; Mourenas et al., 2014; Shi et al., 2018). Mourenas et al. (2012, 2014) and Artemyev et al. (2016) provided the first analytical estimates of bounce-averaged diffusion rates in the presence of oblique waves, and noted their important variation with $\mu_{\max}$. Albert (2017) provided analytical estimates in the limit of large μ, and showed that local diffusion rates are very sensitive to $\mu_{\max}$.

Although the approach originally implemented by Glauert and Horne (2005) is known to be very sensitive to the upper integration limit near the resonance cone, many subsequent studies have used slightly different upper limits. The publicly available version of the Full Diffusion Code, developed at UCLA, uses $X < \tan(0.99\theta_{rc})$ (Shprits & Ni, 2009). Li et al. (2014) estimated $\mu_{\max}$ using a quasi-electrostatic approximation for the hot plasma refractive index (Horne & Sazhin, 1990), and Artemyev et al. (2016) discussed different theoretical estimates of $\mu_{\max}$. Shi et al. (2018) used statistical observations of lower band chorus waves from the Van Allen Probes to provide empirical estimates of $\mu_{\max}$ as a function of L-shell and geomagnetic activity. Some authors have used two constraints on the upper integration limit. Artemyev et al. (2013) used $X < 0.999X_{rc}$ and $\mu < 300$, whilst Mourenas et al. (2014) used $X < 0.995X_{rc}$ and $\mu < 300$. Furthermore, the procedure at the resonance cone is sometimes not reported.

The code developed by Glauert and Horne is called PADIE (Pitch Angle and Energy Diffusion of Ions and Electrons) and is used to calculate diffusion rates for the BAS-RBM. Horne et al. (2013) used the PADIE code to calculate a matrix of bounce-averaged diffusion rates for electron interactions with chorus waves. In a cold plasma $|B_k| \rightarrow 0$ at the resonance cone because the waves become electrostatic. Horne et al. (2013) used Equation 4 to specify the wave spectrum, but ensured that $|B_k| \rightarrow 0$ at the resonance cone by assuming

$$g(\omega, X) = (E_T/E)^2 f(X), \tag{5}$$

where $f(X) = \exp\left(-(X - X_0)^2/X_w^2\right)$ and $\vec{E}_T = \vec{E} - \left(\vec{E}\cdot\vec{k}\right)\vec{k}/k^2$ is the component of the wave electric field transverse to $\vec{k}$. The factor $(E_T/E)^2$ is given by

$$(E_T/E)^2 = \frac{E_y^2 + \left(E_x \cos\theta - E_z \sin\theta\right)^2}{E_x^2 + E_y^2 + E_z^2} = \frac{1 + \left(\frac{\mu^2 - S}{D}\right)^2 \left(\frac{P\cos\theta}{P - \mu^2 \sin^2\theta}\right)^2}{1 + \left(\frac{\mu^2 - S}{D}\right)^2 \left(1 + \left(\frac{\mu^2 \sin\theta\cos\theta}{\mu^2 \sin^2\theta - P}\right)^2\right)}, \tag{6}$$

where the ratios E_x/E_y and E_x/E_z come from the cold plasma dispersion tensor and $\vec{k}$ is assumed to lie in the $x - z$ plane (e.g., Stix, 1992). It is easy to verify that $(E_T/E)^2 = 1$ when $\theta = 0$ and $(E_T/E)^2 = 0$ when $\theta = \theta_{rc}$. As $\theta \rightarrow \theta_{rc}$, $\mu \rightarrow \infty$ and $(E_T/E)^2 \approx \frac{D^2 \sin^4\theta + P^2 \cos^2\theta}{\mu^4 \sin^2\theta}$. Therefore, in this method, the integrand in the expression for $N(\omega)$ scales as $\left(X_{rc}^2(\omega) - X^2\right)^{-1/2}$ which is integrable when $X_{\max} = X_{rc}(\omega)$. Thus, the method of Horne et al. (2013) allows $N(\omega)$ to be calculated with $X_{\max} = X_{rc}(\omega)$. Since $N(\omega)$ approaches a finite value as $X_{\max} \rightarrow X_{rc}(\omega)$, the results are no longer sensitive to small changes in $X_{\max}$. This method was implemented in PADIE in 2013 and has since been used to calculate all the diffusion matrices for the BAS-RBM.

As described above, the method of Horne et al. (2013) assumes that the magnetic wave power decreases as the resonance cone is approached, which is expected from cold plasma theory. However, this assumption is not always consistent with observations. For example, observations of lower band chorus waves from the Van Allen Probes have shown that the magnetic wave power remains roughly constant between $\mu \sim 50$ and $\mu_{\max} \sim 150$, particularly at $L = 4 - 5$ and during quiet to moderate geomagnetic activity (Ma et al., 2017; Shi et al., 2018). In these situations, the method of Horne et al. (2013) could slightly underestimate the magnetic wave power when approaching $\mu_{\max}$. However, the diffusion rate calculations presented in Sections 3 and 4 suggest that the slight underestimation of wave power a few degrees from the resonance cone has a negligible effect on the resulting diffusion rates.

Cunningham (2023) pointed out that the power distribution in $\vec{k}$-space can be converted to the power distribution in (ω, X)-space via a coordinate transformation using the Jacobian. The absolute value of the Jacobian is the ratio of corresponding infinitesimal volume elements in two spaces, for example, $dk_x dk_y dk_z = \left| J\left(\frac{k_x, k_y, k_z}{\omega, X, \phi}\right)\right| d\omega dX d\phi$ (ϕ is an azimuthal coordinate over which symmetry is assumed). Since the wave power in corresponding volume elements must be preserved by the coordinate transformation,

$$\frac{1}{(2\pi)^3}\frac{|B_k|^2}{V} dk_x dk_y dk_z = \frac{1}{4\pi} G(\omega, X) d\omega dX d\phi, \tag{7}$$

where $G(\omega,X)$ denotes the distribution of magnetic wave power in (ω,X)-space. It is convenient to write $G(\omega,X) = B^2(\omega)g(\omega,X)$ because $B^2(\omega)$ is routinely measured by spacecraft. Since $B^2(\omega) = \int_0^\infty G(\omega,X)dX$, it follows that $\int_0^\infty g(\omega,X)dX = 1$ for all frequencies. Substituting the Jacobian into Equation 7 and rearranging yields

$$\frac{|\vec{B}_k|^2}{V} = \frac{B^2(\omega)g(\omega,X)}{\frac{1}{2\pi^2}\frac{k^2X}{\left(1+X^2\right)^{3/2}}\frac{\partial k}{\partial \omega}\Big|_X}, \tag{8}$$

which can be used instead of Equation 4 to specify the wave spectrum in diffusion rate calculations. This method has several advantages. One conceptual advantage is that the function $g(\omega,X)$ is precisely defined as the magnetic spectral density in (ω,X)-space normalized by the total power at each frequency, that is, $g(\omega,X) = G(\omega,X)/B^2(\omega)$. In practical terms, the normalization function $N(\omega)$ does not need to be evaluated, so the diffusion rates can be calculated more efficiently. A detailed comparison of Equations 4 and 8 is given in Cunningham (2023).

Cunningham (2023) calculated local diffusion rates for electron interactions with whistler mode waves using Equations 4 and 8, and showed that the diffusion rates can differ by orders of magnitude if waves propagate very close to the resonance cone. However, PADIE diffusion rates since 2013 have been calculated using the factor of $(E_T/E)^2$ in Equation 5 to mitigate the unsatisfactory behavior at the resonance cone. In this study we compare diffusion rates calculated using three methods to specify the wave spectrum:

1. The method implemented in Glauert and Horne (2005)–Equation 4 and $X_{\max} = \min\left(X_{\max}^{in}, (1-\epsilon)X_{rc}(\omega)\right)$
2. The method implemented in Horne et al. (2013) and used to calculate all PADIE diffusion rates since 2013–Equations 4 and 5
3. Cunningham's formulation–Equation 8

We shall refer to these methods as G&H05, H13 and C23 respectively. We focus on bounce-averaged diffusion rates rather than local diffusion rates; local diffusion rates are calculated at each latitude and averaged over a particle bounce path assuming a dipole field and magnetic moment conservation (Lyons et al., 1972).

2.2. Choice of $g(\omega, X)$

Polarization properties of space plasma waves, including the wave normal angle, are usually studied using multidimensional spectral analysis assuming the presence of a single plane wave. For example, the Singular Value Decomposition (SVD) method (Santolík et al., 2003) has been used to analyze the six dimensional set of orthogonal electric and magnetic field components measured by the EMFISIS instrument on board the Van Allen Probes spacecraft (Kletzing et al., 2023). The SVD method provides a least squares estimate of the wave normal angle as a function of frequency and time, which many studies have used to create a probability density function (PDF) of the wave normal angles (e.g., Agapitov et al., 2013). These distributions necessarily go to zero as $\theta \to 0$ because fewer waves are associated with a shrinking solid angle $\sin\theta d\theta d\phi$ (Li et al., 2013). To account for this, studies have divided the PDF by a factor of $\sin\theta$ before calculating diffusion rates (Artemyev et al., 2016; Mourenas et al., 2014). Using this procedure for lower band chorus waves observed by the Cluster spacecraft, Santolík, Macúšová, et al. (2014) found that PDF/$\sin\theta$ is well approximated by a Gaussian fit centered at the field-aligned direction. Many studies have calculated diffusion rates assuming $g(\omega,X) = f(X)$, where $f(X) = \exp\left(-(X-X_0)^2/X_w^2\right)$ has the form of a Gaussian. In particular, it is customary to take $X_0 = 0$ to model a wave spectrum peaked in the field-aligned direction. Diffusion rates calculated using the PADIE code since 2013 have used $g(\omega, X) = (E_T/E)^2 f(X)$ as described in Section 2.1.

In Cunningham's formulation $g(\omega, X)$ is precisely defined as the magnetic spectral density in (ω, X)-space normalized by the total power at each frequency (see Section 2.1), so it is appropriate to use a power-weighted PDF as $g(\omega, X)$. Since these PDFs have been divided by $\sin\theta$ and approximated by a Gaussian $f(X) = \mathrm{PDF}/\sin\theta$, we choose to use $g(\omega, X) \sim \sin\theta f(X) = Xf(X)/\sqrt{1+X^2}$. Including the normalizing constant, $g(\omega, X) = A(\omega)Xf(X)/\sqrt{1+X^2}$, where $A(\omega) = 1/\int_{X_{\min}}^{X_{\max}(\omega)} Xf(X)/\sqrt{1+X^2}\,dX$. In Cunningham's formulation it is important to use a form of $g(\omega, X)$ that satisfies $g(\omega, X = 0) = 0$, otherwise $|B_k|^2/V \to \infty$ as $X \to 0$. If $|B_k|^2/V$ is constant within a small neighborhood of $X = 0$, Equation 8 suggests that $g(\omega, X) \sim X$. Cunningham (2023) suggested using $g(\omega, X) \sim Xf(X)$. Note that our choice of $g(\omega, X)$ also satisfies $g(\omega, X) \sim X$ near $X = 0$.

In summary, each of the 3 methods use a different form of $g(\omega, X)$:

1. G&H05: $g(\omega, X) = f(X)$
2. H13: $g(\omega, X) = (E_T/E)^2 f(X)$
3. C23: $g(\omega, X) = A(\omega)Xf(X)/\sqrt{1+X^2}$, $A(\omega) = 1/\int_{X_{\min}}^{X_{\max}(\omega)} Xf(X)/\sqrt{1+X^2}\,dX$

In all methods $X_{\min} \le X \le X_{\max}(\omega)$ and $f(X) = \exp\left(-(X - X_0)^2/X_w^2\right)$.

2.3. Distribution of Wave Power in Each Method

Calculating a local quasi-linear diffusion rate using Equation 1 involves a sum over harmonic integers n and an integral over $X = \tan\theta$. As described in Section 2.1, the integrand is proportional to the magnetic power spectral density $|B_k|^2/V$. Since the three methods differ only in the expression for $|B_k|^2/V$, it is instructive to compare the wave distributions between the methods directly, rather than the resulting diffusion rates. Cunningham (2023) showed that the magnetic wave power per unit frequency is preserved by both Equations 4 and 8; the difference is the weighting of wave energy over wave normal angle (WNA). In this section we introduce the effective WNA distribution, which will be used in Sections 3 and 4 to compare the weighting of wave energy with respect to X between the three methods under consideration.

We define the effective WNA distribution

$$g_{\text{effective}}(\omega, X) = \frac{1}{2\pi^2}\frac{1}{B^2(\omega)}\frac{k^2 X}{\left(1+X^2\right)^{3/2}}\left.\frac{\partial k}{\partial \omega}\right|_X \frac{|\vec{B}_k|^2}{V}, \tag{9}$$

where the form of $|B_k|^2/V$ depends on the chosen method from Section 2.1. The effective WNA distribution is the distribution of magnetic wave power in (ω, X)-space, normalized by the total power spectral density $B^2(\omega)$ at that frequency. Since that is the definition of $g(\omega, X)$ in Cunningham's formulation, $g_{\text{effective}}(\omega, X) = g(\omega, X)$ for method C23. This is easily verified by substitution of Equation 8 into Equation 9. Since $g_{\text{effective}}(\omega, X) = g(\omega, X)$, method C23 is exact if the distribution of magnetic wave power in (ω, X)-space can be determined directly, for example, in a numerical simulation (Cunningham, 2023).

Although methods G&H05 and H13 do not transform directly between $\vec{k}$-space and (ω, X)-space via the Jacobian, they still produce an effective distribution in (ω, X)-space by specifying $|B_k|^2/V$. Substitution of Equation 4 into Equation 9 yields

$$g_{\text{effective}}(\omega, X) = \frac{1}{2\pi^2}\frac{k^2 X}{\left(1+X^2\right)^{3/2}}\left.\frac{\partial k}{\partial \omega}\right|_X \frac{g(\omega, X)}{N(\omega)}, \tag{10}$$

which is the effective WNA distribution for methods G&H05 and H13 (depending on whether the factor of $(E_T/E)^2$ is included in $g(\omega, X)$). By the definition of $N(\omega)$, the integral of Equation 10 over X is unity. In Cunningham's formulation $g_{\text{effective}}(\omega, X) = g(\omega, X)$ and $\int_0^\infty g(\omega, X)\,dX = 1$ for all frequencies, therefore $\int_0^\infty g_{\text{effective}}(\omega, X)\,dX = 1$ in all three methods.

3. Test Calculations for Chorus Waves

Chorus waves are important, naturally occurring electromagnetic waves that propagate in the whistler mode and drive both acceleration and loss of radiation belt electrons (Thorne et al., 2010, 2013). They are typically observed in two distinct frequency bands, a lower band and an upper band, separated by a gap at one half of the local electron gyrofrequency (Gao et al., 2019). In this section, we calculate bounce-averaged diffusion rates using input parameters representative of lower and upper band chorus waves. We consider a range of electron kinetic energies $E = 10$ keV, 100 keV, 200 keV, 500 keV, 1 MeV, 2 MeV, and 5 MeV. Other wave types are addressed in Section 4.

3.1. Input Parameters

For simplicity we keep many of the input parameters the same for lower and upper band chorus. We consider an electron-proton plasma at $L = 4$ in a dipole magnetic field, which corresponds to an equatorial electron cyclotron frequency $\Omega_e^{eq} = 8.574 \times 10^4$ rad s^{-1}. The ratio of the electron plasma frequency to the electron cyclotron frequency is taken to be $\omega_{pe}/\Omega_e^{eq} = 1.5$ at the equator, which is a low density for observations in the inner magnetosphere (Daggitt et al., 2024; Horne et al., 2024). The cold plasma density is assumed constant with latitude so the local value of ω_{pe}/Ω_e decreases away from the equator. We focus on low densities for two reasons: first, stochastic acceleration of electrons is enhanced in regions of low density (Allison et al., 2021); second, Cunningham suggested that his method could lead to more significant differences when ω_{pe}/Ω_e is low. The harmonic resonances considered are from $n = -10, \ldots, +10$ and the form of $g(\omega, X)$ used in each method is described in Section 2.2. Following Horne et al. (2013), the wave spectrum is peaked in the field-aligned direction with $X_0 = 0.0$ at all latitudes, and waves are restricted to propagate between $X_{\min} = 0.0$ and $X_{\max}^{in} = 1.15$, although $X_{\max}$ is adjusted as described in Section 2.1 if the resonance cone angle becomes less than $X_{\max}^{in}$. We take $X_w = 0.35$ which is typical of chorus wave normal angle observations (Santolík, Macúšová, et al., 2014).

The frequency spectrum and latitudinal extent are different for lower and upper band chorus. The power spectral density is taken to be a Gaussian, peaked at ω_0 and with width $\delta\omega$, truncated at ω_{lc} and ω_{uc} such that $\int_{\omega_{lc}}^{\omega_{uc}} B^2(\omega)d\omega = B_{wave}^2$ (Glauert & Horne, 2005). We take $B_{wave} = 100$ pT but note that the diffusion rates are proportional to B_{wave}^2, so varying B_{wave} amounts to multiplying all the diffusion rates by a constant. For lower band chorus we take $\omega_{lc} = 0.1\Omega_e^{eq}$, $\omega_{uc} = 0.5\Omega_e^{eq}$, $\omega_0 = 0.35\Omega_e^{eq}$ and $\delta\omega = 0.15\Omega_e^{eq}$. The values for upper band chorus are $\omega_{lc} = 0.5\Omega_e^{eq}$, $\omega_{uc} = 0.7\Omega_e^{eq}$, $\omega_0 = 0.6\Omega_e^{eq}$ and $\delta\omega = 0.1\Omega_e^{eq}$. Following Horne et al. (2013), the lower band chorus is bounce-averaged between magnetic latitudes $0 < |\lambda_m| < 42°$, whilst the upper band chorus is assumed to exist between $0 < |\lambda_m| < 12°$.

3.2. Results

The results for lower band chorus are presented in Figure 1. The columns contain the diffusion rates in pitch angle (left), energy (middle) and mixed pitch angle-energy (right), and the rows have increasing electron kinetic energy from top to bottom. The results for $E = 10$ keV are omitted because there are no resonant interactions for the chosen input parameters, so the diffusion rates are equal to zero. Methods G&H05, H13 and C23 correspond to the red, black and cyan lines respectively. Figure 1 shows that there is very little difference between the methods for input parameters typical of lower band chorus waves.

To quantify how different methods G&H05 and H13 are from method C23, let $D_{\alpha\alpha}^m$ denote the diffusion rate calculated using method m and define the multiplicative deviation factor for pitch-angle diffusion

$$F_{\alpha\alpha}^m(\alpha, E) = \exp\left|\log\left|\frac{D_{\alpha\alpha}^m(\alpha, E)}{D_{\alpha\alpha}^{\mathrm{C23}}(\alpha, E)}\right|\right|, \quad m = \mathrm{G\&H05 \text{ or } H13}. \tag{11}$$

By definition $F_{\alpha\alpha}^m \geq 1$, and $F_{\alpha\alpha}^m = 1$ if $D_{\alpha\alpha}^m = D_{\alpha\alpha}^{\mathrm{C23}}$. Hence $F_{\alpha\alpha}^m$ is the multiplicative factor by which $D_{\alpha\alpha}^m$ differs from $D_{\alpha\alpha}^{\mathrm{C23}}$, irrespective of which diffusion rate is greater. The corresponding factors F_{EE}^m and $F_{\alpha E}^m$ for energy and mixed diffusion are defined similarly. We calculate F^m for all our test calculations and consider the 95th percentile combining pitch angle, energy and mixed diffusion: $P_{95}^m = \mathrm{percentile}_{95}\,\{F_{\alpha\alpha}^m, F_{EE}^m, F_{\alpha E}^m\}$. For lower band

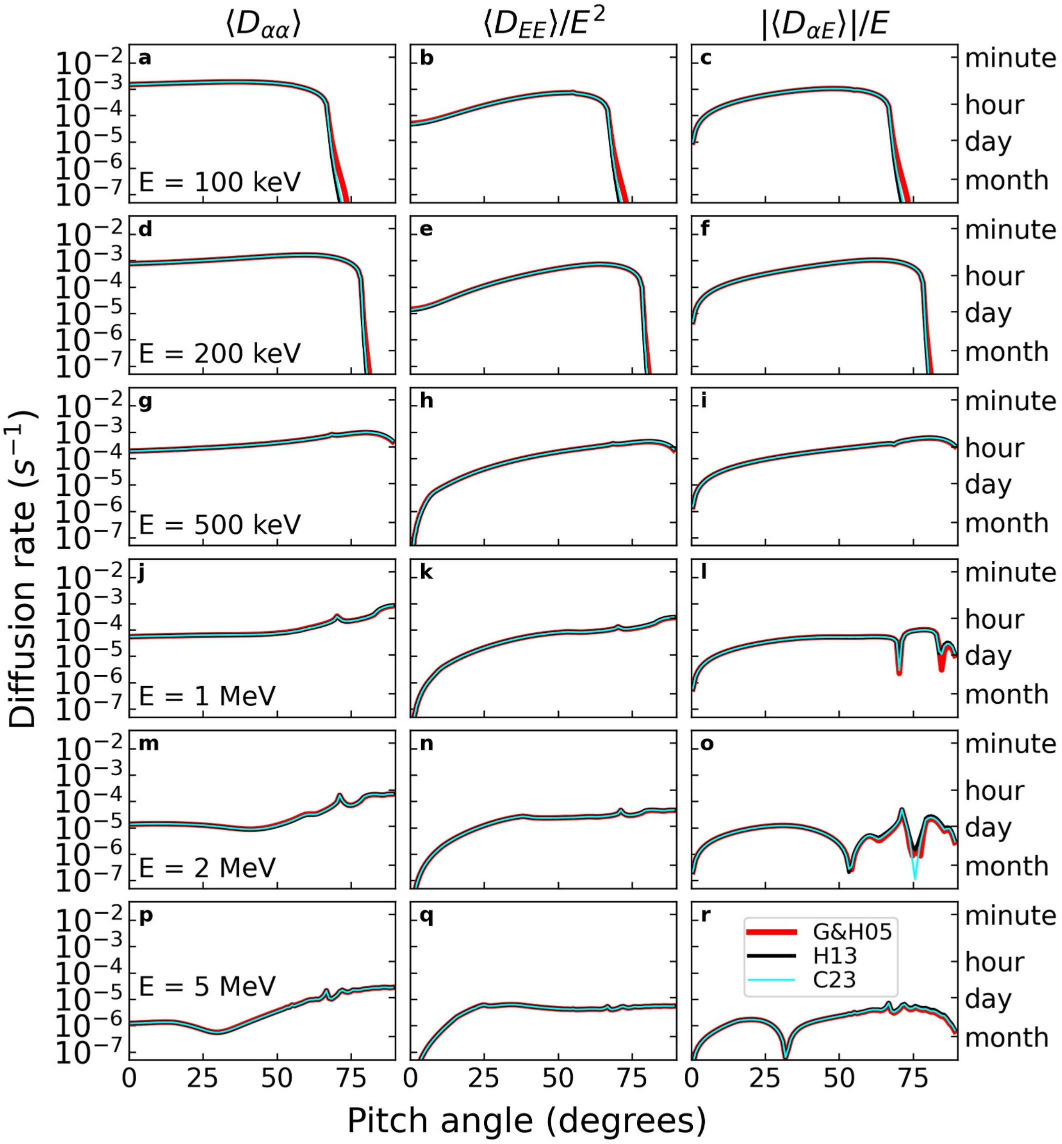

Figure 1. Bounce-averaged pitch angle (left), energy (middle) and mixed pitch angle-energy (right) diffusion rates for resonant interactions of electrons with lower band chorus waves using three different methods to specify the wave spectrum: G&H05 (red), H13 (black) and C23 (cyan). The electron kinetic energy increases from top to bottom.

chorus we obtain $P_{95}^{\mathrm{G\&H05}} = 1.09$ and $P_{95}^{\mathrm{H13}} = 1.10$. Since the diffusion rates vary over several orders of magnitude, a factor of 1.1 is a negligible difference.

Figure 2 presents the results for upper band chorus in the same style as Figure 1, except that Figure 2 contains an extra row to include the results for $E = 10$ keV. Method G&H05 differs from method C23 by several orders of magnitude at some pitch angles, particularly at low energies. However, the differences between methods H13 and C23 are very small. We repeat the analysis described above to quantify the differences and obtain $P_{95}^{\mathrm{G\&H05}} = 87.6$ and $P_{95}^{\mathrm{H13}} = 1.64$ for upper band chorus. A factor of 87.6 between methods G&H05 and C23 could have serious implications for global diffusion models of the radiation belts. In contrast, a factor of 1.64 between methods H13 and C23 is negligible compared to other uncertainties in the initial conditions, boundary conditions and the averaging over the natural variability of the waves. We note that all the diffusion rates used in the BAS-RBM were calculated using method H13, so calculating diffusion rates using method C23 is unlikely to produce significant changes in the predicted radiation belt electron flux.

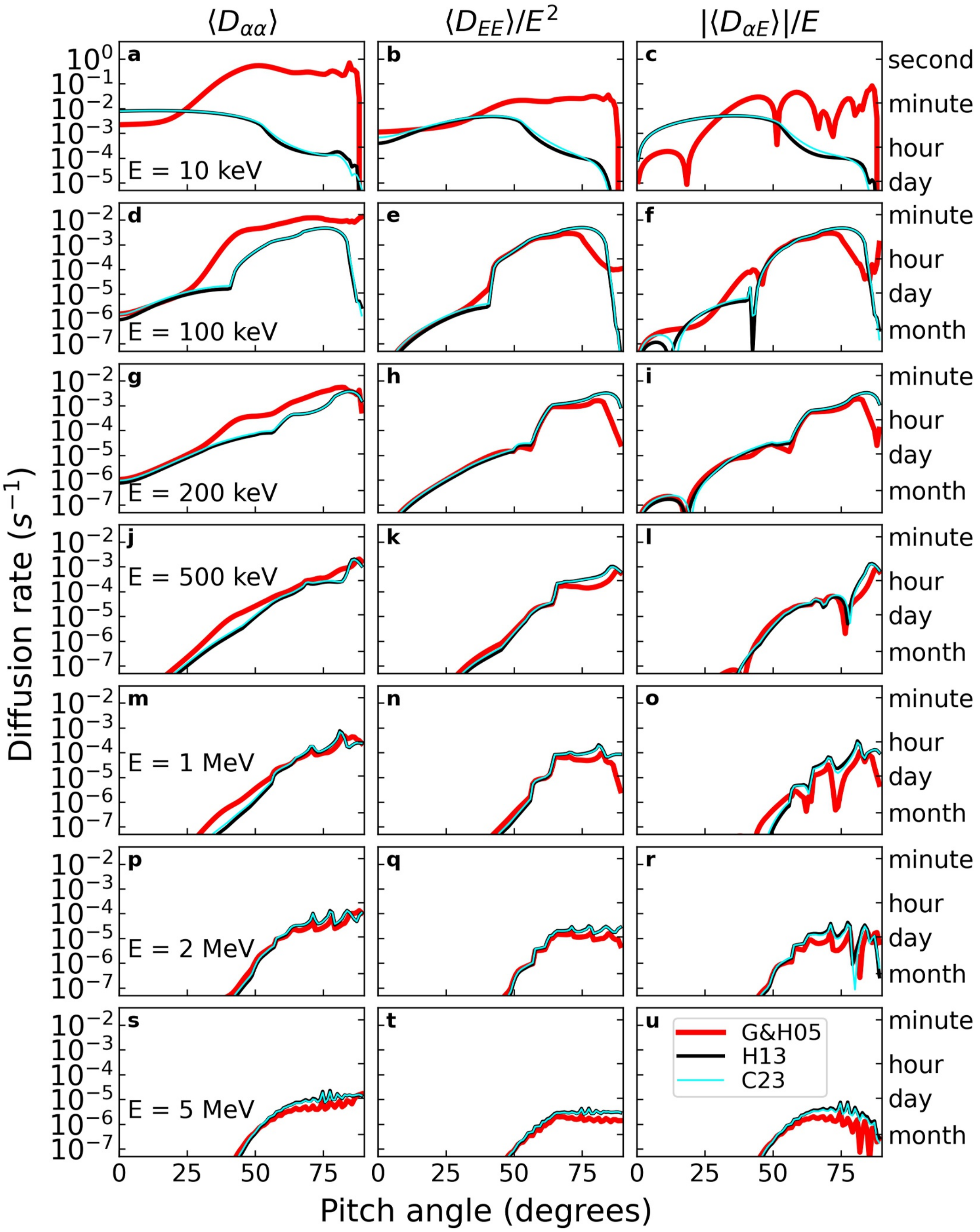

Figure 2. Bounce-averaged pitch angle (left), energy (middle) and mixed pitch angle-energy (right) diffusion rates for resonant interactions of electrons with upper band chorus waves using three different methods to specify the wave spectrum: G&H05 (red), H13 (black) and C23 (cyan). The electron kinetic energy increases from top to bottom and the top row has a y-axis scale two orders of magnitude greater than the other rows.

3.3. Proximity to the Resonance Cone

Cunningham (2023) found significant differences in local diffusion rates between methods G&H05 and C23 when waves propagate near the resonance cone angle. For our test calculations $X_{rc}\left(\omega = 0.5\Omega_e^{eq}\right) = 1.42$ at the equator. Note that $X_{rc}(\omega)$ decreases with increasing ω, so 1.42 is the smallest value of $X_{rc}(\omega)$ in the lower band chorus frequency range. In our model the resonance cone angle increases away from the equator, so 1.42 is the smallest value of the resonance cone at any frequency or latitude for our lower band chorus calculations. Since the

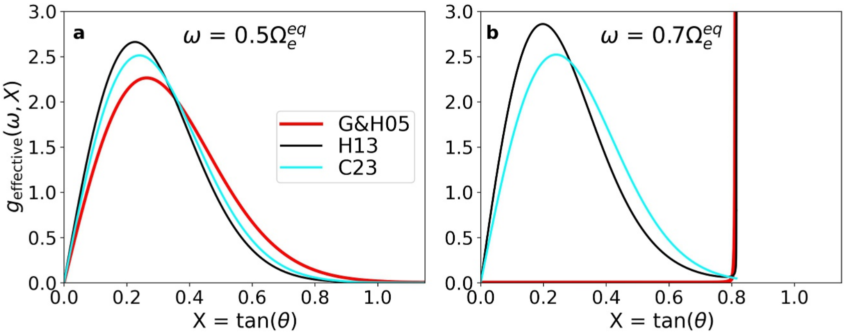

Figure 3. The effective wave normal angle distribution (defined in Section 2.3) for whistler waves with $\omega = 0.5\Omega_e^{eq}$ (left) and $\Omega = 0.7\omega_e^{eq}$ (right).

waves are restricted to $X_{\max} = 1.15$ they do not propagate near the resonance cone. Therefore, the lower band chorus calculations do not enter the regime where Cunningham found the largest differences.

The test calculations for upper band chorus extend to $\omega_{uc} = 0.7\Omega_e^{eq}$, for which the resonance cone angle at the equator is $X_{rc}\left(\omega = 0.7\Omega_e^{eq}\right) = 0.82$. In this case $X_{\max}$ is adjusted to $\leq X_{rc}(\omega)$ as described in Section 2.1 and waves propagate very close to the resonance cone. Our results for upper band chorus show significant differences between methods G&H05 and C23, as found by Cunningham. However, method H13 differs from method C23 by a factor of 1.64 at the 95th percentile, showing that method H13 effectively mitigates issues at the resonance cone.

3.4. Comparing the Wave Spectrum for Each Method

The effective wave normal angle distribution (defined in Section 2.3) for each of the three methods is shown in Figure 3 for the input parameters at the equator in our test calculations. Figures 3a and 3b show $g_{\text{effective}}(\omega, X)$ as a function of X at fixed frequencies $\omega = 0.5\Omega_e^{eq}$ and $\omega = 0.7\Omega_e^{eq}$ respectively. As described in Section 3.3, waves with $\omega = 0.5\Omega_e^{eq}$ do not propagate near the resonance cone. Figure 3a shows the effective WNA distribution is similar between the three methods, so the distribution of wave power in (ω, X)-space is similar for each method. This remains true for the range of frequencies included in the lower band chorus calculations and explains the agreement in the resulting diffusion rates ($P_{95}^{\text{G\&H05}} = 1.09$ and $P_{95}^{\text{H13}} = 1.10$).

For $\omega = 0.7\Omega_e^{eq}$, $X_{\max}$ is adjusted to $\leq X_{rc} = 0.82$ (see Section 3.3). Figure 3b shows that the magnetic wave power becomes highly peaked at the resonance cone in method G&H05, which was also stated by (Cunningham, 2023). This is not satisfactory because probability density functions of observed chorus wave normal angles exhibit a peak at $\sim 10°$, which is sometimes referred to as a quasi-parallel population (Li et al., 2016). The unsatisfactory behavior at the resonance cone affects the G&H05 method calculations for upper band chorus. Method C23 has an effective WNA distribution which peaks at $X \sim 0.25$ and decreases to a small finite value at the resonance cone, which models the quasi-parallel population of chorus waves. The totally different distribution of magnetic wave power between methods G&H05 and C23 results in diffusion rates that can differ by more than an order of magnitude $\left(P_{95}^{\text{G\&H05}} = 87.6\right)$. However, the distribution of wave power in (ω, X)-space remains similar between methods H13 and C23, which explains the small differences in the diffusion rates $\left(P_{95}^{\text{H13}} = 1.64\right)$.

The one striking difference between methods H13 and C23 in Figure 3b is at the resonance cone X_{rc}; here $g_{\text{effective}}(\omega, X)$ for method H13 diverges to infinity. This is because the Jacobian scales as μ^5 near the resonance cone, whilst $(E_T/E)^2 \sim \mu^{-4}$, giving $g_{\text{effective}} \sim \mu$. However, it is evident from Figure 2 that the resulting diffusion rates are not affected. This is because the rapid increase in $g_{\text{effective}}(\omega, X)$ near the resonance cone for method H13 only accounts for a very small fraction of the magnetic wave power at that frequency; the majority of wave power is distributed over $0 < X < 0.8$ (black line in Figure 3b). Therefore, the total diffusion rate in methods H13 and C23 is dominated by lower order harmonic resonances, which produce resonant interactions away from the resonance cone. This is demonstrated in Appendix A for $E = 10$ keV, where the $n = -1$ resonance dominates the total diffusion rate in methods H13 and C23. Away from the resonance cone, Figure 3b shows that the weighting of wave energy is very similar between methods H13 and C23, which is why the diffusion rates exhibit only very small differences.

Appendix A also shows that higher order harmonics produce interactions closer to the resonance cone, and the diffusion rate from higher order harmonics in method H13 can exceed method C23 by a factor of ~ 3. However, since higher order harmonics have a small contribution to the total diffusion rate, these differences are not seen in Figure 2. Higher order harmonics could become important in methods H13 and C23 for input parameters representing obliquely propagating chorus waves, since this would place more magnetic wave power at large WNAs. Li et al. (2016) observed oblique lower band chorus waves propagating with WNAs between the Gendrin angle and the resonance cone angle. However, the quasi-parallel population of chorus waves accounts for the majority of the magnetic wave power. Wong et al. (2023) separated chorus wave observations from the Van Allen Probes into small and large WNA populations and calculated diffusion rates for each population separately. Chorus waves with small WNAs were found to have the dominant contribution to the total diffusion rate, and we have shown that quasi-parallel (small WNA) lower band chorus waves exhibit very small differences between the methods. Therefore, although methods H13 and C23 could exhibit greater differences for oblique lower band chorus, the total lower band chorus diffusion rate is unlikely to differ significantly. Since oblique lower band chorus propagates close to the resonance cone, the magnetic wave power will be highly peaked at the resonance cone in method G&H05. Therefore, using method G&H05 for oblique lower band chorus is likely to result in significant differences compared to method C23.

4. Other Wave Types

4.1. Hiss Waves

Hiss waves are whistler mode waves that drive electron pitch-angle scattering in the slot region (Lyons & Thorne, 1973). We adopt the hiss wave model of Ni et al. (2013) for our test calculations. The frequency spectrum is given by $f_0 = 550$ Hz, $\delta f = 300$ Hz, $f_{lc} = 100$ Hz and $f_{uc} = 2000$ Hz at all latitudes. Hiss waves are assumed to exist between $0^\circ < |\lambda_m| < 45^\circ$ and the WNA distribution varies across 9 latitude bins of width 5°. The peak WNA varies from $X_0 = 0$ at the equator to $X_0 = \tan(80^\circ) = 5.67$ at high latitudes, and the full details of the WNA inputs at each latitude are available in Table 1 of Ni et al. (2013). Since hiss waves are observed inside the high-density plasmasphere we take $f_{pe}/f_{ce}^{eq} = 10$. The broadband amplitude is $B_{wave} = 30$ pT, and the other parameters are the same as for the chorus wave calculations. Figure 4 presents the bounce-averaged diffusion rates for hiss waves, showing that the differences between the three methods are very small. We repeat the analysis from Section 3.2 and obtain $P_{95}^{\mathrm{G\&H05}} = 1.05$ and $P_{95}^{\mathrm{H13}} = 1.24$ for the 95th percentile of the multiplicative deviation factor. As argued previously, these are minor differences considering the diffusion rates vary over several orders of magnitude.

The effective wave normal angle distribution for hiss waves at $\lambda_m = 0^\circ$ and $\lambda_m = 45^\circ$ is plotted in Figures 5a and 5b respectively. At the equator $X_0 = 0$ and the waves propagate quasi-parallel to the background magnetic field in our model. Although the effective WNA distribution goes to zero at $X = 0$ due the factor of X in the Jacobian (see Section 2.2), the power spectral density in wavevector space is peaked in the field-aligned direction. Figure 5a shows that the effective WNA distribution at the equator is near-identical for each method, so it follows that the differences in the local diffusion rates are negligible at the equator. At higher latitudes, ray tracing simulations and observations suggest that the peak wave power moves to larger WNAs (Ni et al., 2013). In our test calculations, $X_0 = \tan(80^\circ) = 5.67$ at magnetic latitude $\lambda_m = 45^\circ$. Figure 5b shows that differences arise in the effective WNA distributions. In particular, the wave spectrum for method H13 is weighted more toward parallel propagation by the factor of $(E_T/E)^2$. The hiss wave spectrum for method G&H05 (red) is closer to method C23 (cyan) than method H13 (black), which explains why we obtained $P_{95}^{\mathrm{G\&H05}} < P_{95}^{\mathrm{H13}}$.

Note that the resonance cone X_{rc} does not become less than the inputted $X_{\max}^{in}$ for our hiss wave calculations. Hiss waves are observed inside the plasmasphere and are more oblique at higher latitudes. However, X_{rc} increases at lower L and higher latitude. Therefore, the regions where hiss waves propagate more obliquely are also regions where the resonance cone angle is larger. It is possible that issues at the resonance cone could occasionally affect method G&H05 in a similar way to the chorus wave calculations, but we argue this is unlikely given the typically observed hiss wave properties.

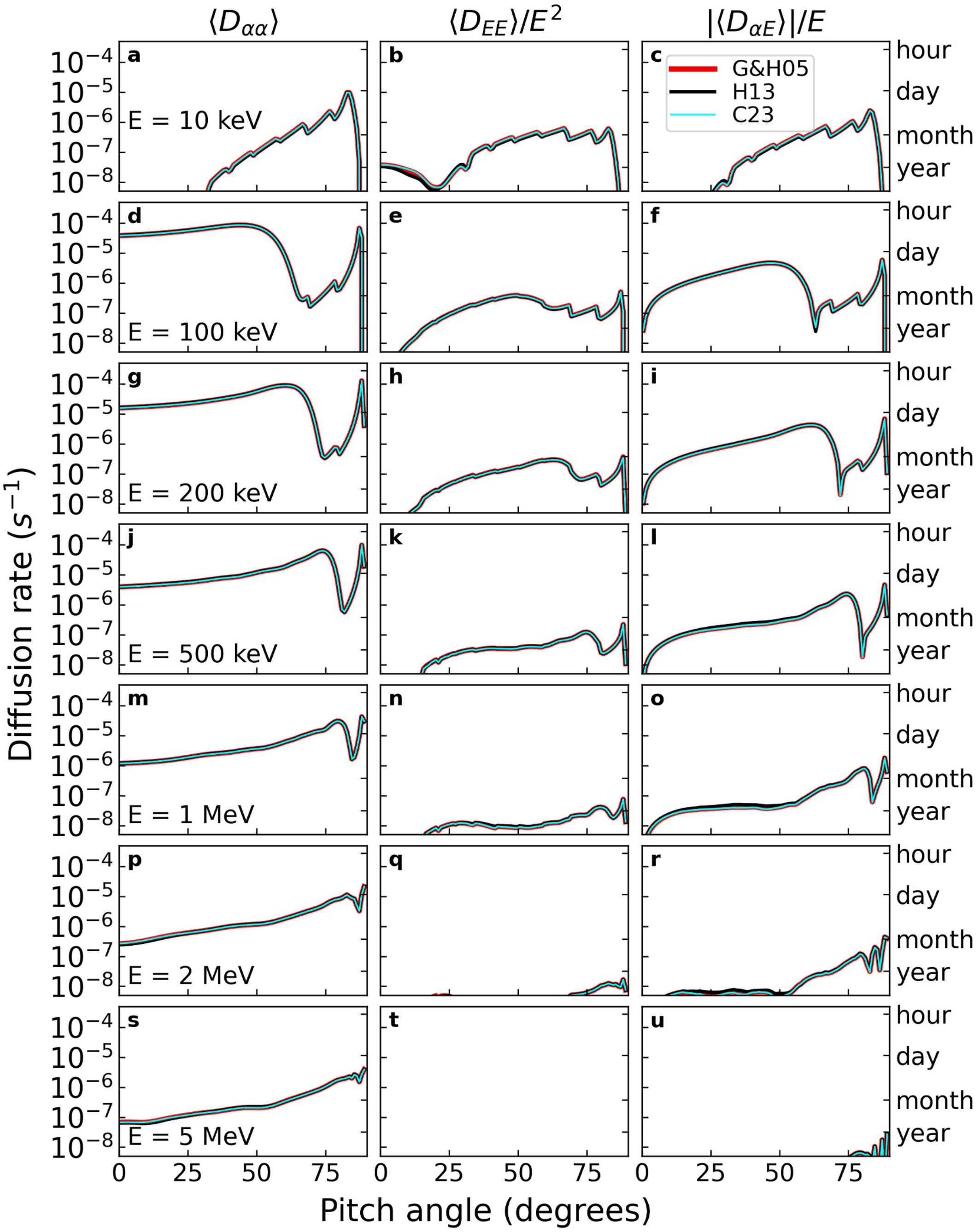

Figure 4. Bounce-averaged pitch angle (left), energy (middle) and mixed pitch angle-energy (right) diffusion rates for resonant interactions of electrons with hiss waves. The electron kinetic energy increases from top to bottom.

4.2. Electromagnetic Ion Cyclotron Waves

EMIC waves drive losses of multi-MeV electrons via pitch-angle scattering into the loss cone (Lyons & Thorne, 1972; Meredith et al., 2003). Many studies have modeled EMIC waves using quasi-linear theory (e.g., Lyu et al., 2024). EMIC waves propagate primarily parallel to the magnetic field and the resonance cone is very large unless the wave frequency is just below one of the ion cyclotron frequencies. The diffusion rates used in the BAS-RBM were calculated by Ross et al. (2020, 2021) using the constraint $\omega/\Omega_i < 0.97$ to limit the wave frequency relative to the ion cyclotron frequency. Ross et al. also assumed a quasi-parallel EMIC wave spectrum using $X_0 = 0$, $X_w = \tan(15°)$ and $X_{\max} = 2X_w = 0.54$. Therefore, X_{rc} is much larger than $X_{\max}$ and issues at the

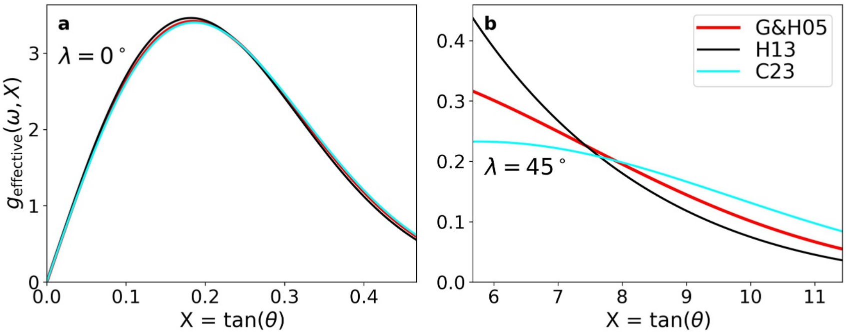

Figure 5. The effective wave normal angle distribution for hiss waves at frequency $f = 550$ Hz and magnetic latitude $\lambda_m = 0°$ (a) and $\lambda_m = 45°$ (b) using three different methods to specify the wave spectrum: G&H05 (red), H13 (black) and C23 (cyan). The input values are $X_0 = 0$, $X_w = \tan(15°)$, $X_{\min} = 0$, $X_{\max} = \tan(25°)$ for $\lambda_m = 0°$, and $X_0 = \tan(80°)$, $X_w = \tan(80°)$, $X_{\min} = \tan(80°)$, $X_{\max} = \tan(85°)$ for $\lambda_m = 45°$.

resonance cone do not affect method G&H05. Taking an electron-proton plasma with $\omega_{pe}/\Omega_e = 10$ and a background field strength at $L = 4$ in a dipole, Figure 6 shows the effective WNA distribution for $\omega = 0.97\Omega_{H^+}$, where Ω_{H^+} is the proton cyclotron frequency. Since the effective WNA distributions in Figure 6 are near-identical, it follows that differences in the resulting diffusion rates will be negligible.

4.3. Fast Magnetosonic Waves

Fast magnetosonic waves are observed near the equator and propagate on the whistler branch at large wave normal angles, with frequencies between the proton cyclotron frequency and the lower hybrid frequency (Santolík et al., 2004). Horne et al. (2007) calculated bounce-averaged quasi-linear diffusion rates for fast magnetosonic waves observed by the Cluster 3 spacecraft and suggested that Landau resonant interactions can contribute to electron acceleration in the outer radiation belt. Wong et al. (2022) used data from the Van Allen Probes to calculate bounce- and drift-averaged diffusion rates for the BAS-RBM, and found that although chorus waves are the dominant driver of energy diffusion in the outer belt, magnetosonic waves contribute to electron losses in the slot region.

We calculate bounce-averaged diffusion rates for magnetosonic waves using the input parameters of Horne et al. (2007), which were obtained from Cluster 3 data. The Gaussian frequency spectrum is given by $\omega_0/\Omega_e^{eq} = 3.49 \times 10^{-3}$, $\delta\omega/\Omega_e^{eq} = 8.86 \times 10^{-4}$, $\omega_{lc}/\Omega_e^{eq} = 0.0026$, $\omega_{uc}/\Omega_e^{eq} = 0.0044$, and $B_{wave} = 218$ pT. The waves exist at $|\lambda_m| < 3°$ and $L = 4.5$, $\omega_{pe}/\Omega_e^{eq} = 3.0$, and we consider the same range of energies as in Section 3. Since the wave normal angle was determined to be approximately $\theta = 89°$, Horne et al. (2007) used $X_0 = \tan(89°)$, $X_w = \tan(86°)$, $X_{\min} = X_0 - 2X_w$ and $X_{\max} = X_0 + 2X_w$ for the wave normal angle inputs.

Figure 7 presents the bounce-averaged diffusion rates for magnetosonic waves. The results for $E = 10$ keV are omitted because there are no resonant interactions and the diffusion rates are equal to zero. Methods G&H05 and H13 produce almost identical diffusion rates across all (α, E); however, they differ from method C23 by a factor of 2–3 at some (α, E). To quantify the differences, we repeat the analysis from Section 3.2 and obtain $P_{95}^{\text{G\&H05}} = 2.76$ and $P_{95}^{\text{H13}} = 2.95$ as the 95th percentile of the multiplicative deviation factors. Although these differences are larger than for the other wave modes, we explain in Section 5 that they are within the uncertainties associated with the input parameters. Furthermore, diffusion rates due to other wave modes tend to dominate over magnetosonic waves at most (α, E, L) (Glauert et al., 2024; Wong et al., 2022). Therefore, many global radiation belt models omit the effect of fast magnetosonic waves.

The results can be understood by comparing the distribution of wave energy using the effective wave normal angle distribution, which is plotted in Figure 8 for the input parameters at the equator in our test calculations. The

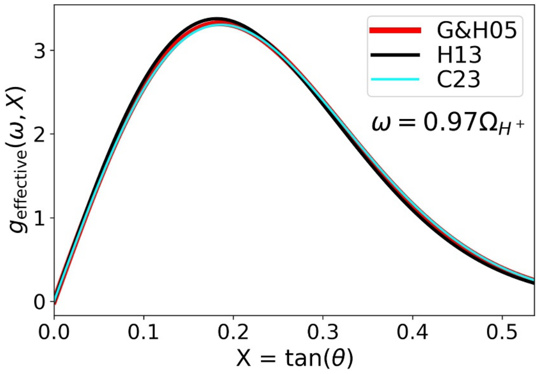

Figure 6. The effective wave normal angle distribution for electromagnetic ion cyclotron waves with $\omega = 0.97\Omega_{H^+}$ and using three different methods to specify the wave spectrum: G&H05 (red), H13 (black) and C23 (cyan).

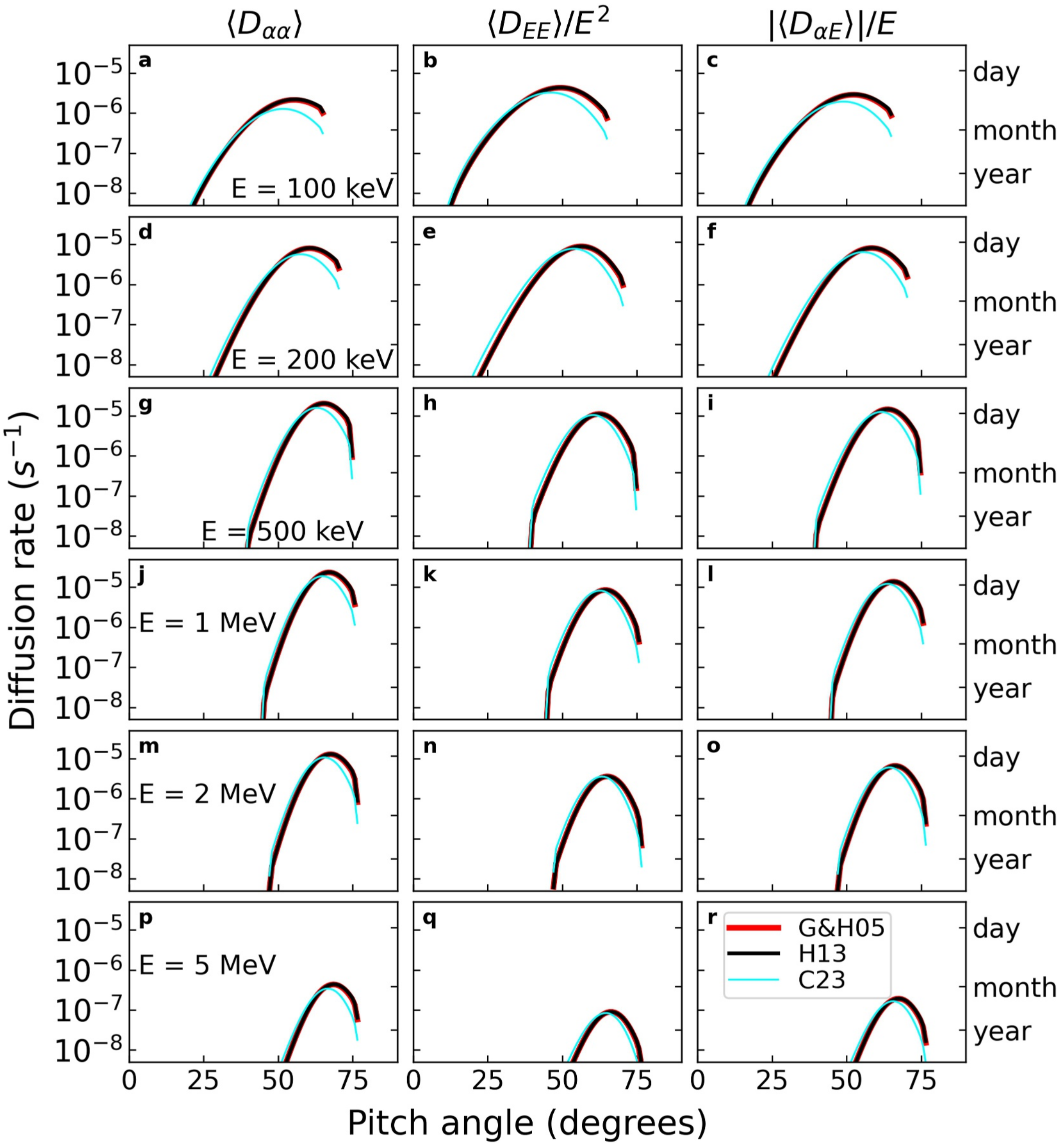

Figure 7. Bounce-averaged pitch angle (left), energy (middle) and mixed pitch angle-energy (right) diffusion rates for resonant interactions of electrons with fast magnetosonic waves using three different methods to specify the wave spectrum: G&H05 (red), H13 (black) and C23 (cyan). The electron kinetic energy increases from top to bottom.

effective WNA distribution is almost identical for methods G&H05 and H13, which explains why the diffusion rates are almost identical. However, the distribution of wave energy in method C23 is slightly different, with the peak shifted to slightly larger X. As $\theta \rightarrow 90°$, $X = \tan\theta$ is very sensitive to small changes in θ, so the peak is shifted by a very small amount in θ-space. Although Figure 8 only shows the effective WNA distribution at a single fixed frequency $\omega = \omega_0$ and magnetic latitude $\lambda_m = 0°$, it is very similar across the range of frequencies and latitudes included in these test calculations. Since fast magnetosonic waves propagate below the lower hybrid frequency, there is no whistler-mode resonance cone at these frequencies, so method G&H05 is not be affected by issues at the resonance cone.

4.4. VLF Transmitter Waves

Anthropogenic whistler waves originating from ground-based VLF transmitters can interact with radiation belt electrons at low L-shells. However, these waves typically have a narrow angular spread. For example, Ross et al. (2019) calculated quasi-linear diffusion rates due to VLF transmitters using $X_w = \tan(10°) = 0.176$ and

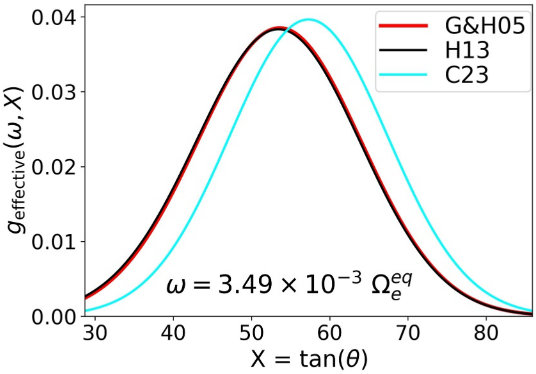

Figure 8. The effective wave normal angle distribution for fast magnetosonic waves with $\omega/\Omega_e^{eq} = 3.49 \times 10^{-3}$ and using three different methods to specify the wave spectrum: G&H05 (red), H13 (black) and C23 (cyan).

Selesnick et al. (2013) used a narrow band formulation of quasi-linear theory where waves propagate at a single frequency and wave normal angle at each latitude. Cunningham (2023) pointed out that Equations 4 and 8 will give almost identical results if X_w is small; the results are identical if $g(\omega, X) = \delta(X - X_0)$. Therefore, the diffusion rates due to VLF transmitters are unlikely to differ significantly between the three methods.

5. Discussion and Implications

The magnetic wave power per unit frequency is the same in each method under consideration; the difference is the weighting of wave energy with respect to wave normal angle (see Section 2.3). In this context, it is important to consider the assumptions and approximations that underlie the quasi-linear diffusion rates. Quasi-linear theory assumes that the wave spectrum is broadband and incoherent so that particle motion is stochastic and the distribution function evolves according to the diffusion equation (Lyons & Williams, 1984). Observed wave spectra are averaged over space and time to obtain the input parameters for the diffusion rates. In reality, wave properties are highly variable and the input $g(\omega, X)$ is usually estimated by considering a power-weighted PDF of the observed WNAs (Wong et al., 2023). As described in Section 2.2, the method used to determine the WNA assumes the presence of a single plane wave. The underlying assumptions of quasi-linear theory, approximations involved in measuring the wave normal angle and the averaging over many events are bound to lead to some uncertainty. Slight redistribution of wave energy with respect to wave normal angle is within this level of uncertainty. In fact, rather than using statistics of observed WNAs, many studies have used nominal values for the wave normal angle inputs (Horne et al., 2013; Kersten et al., 2014; Ross et al., 2021; Wong et al., 2022). In this case the WNA input values have been assumed, so small variations in the angular distribution of wave energy are acceptable.

We have presented the distribution of wave energy with respect to X using the effective WNA distribution. The effective WNA distribution depends on the dispersion relation, and thus the input parameters for the local diffusion rate calculation. We have used input parameters that are typical of wave types that have been used to calculate diffusion rates for the BAS-RBM. If $X_0 = 0$ and $X_{\max} \ll X_{rc}(\omega)$, the effective WNA distribution is almost identical between the methods, for example, in the case of EMIC waves (Figure 6) and hiss waves at the equator (Figure 5a). If $X_0 > 0$ and $X_{\max} \ll X_{rc}(\omega)$, the three methods have slightly different distributions of wave energy with respect to WNA. This could occur for hiss waves at high latitudes (Figure 5b) or fast magnetosonic waves (Figure 8). However, given the approximations and averaging procedures involved in calculating quasi-linear diffusion rates, slight variations in the angular distribution of wave energy are within the uncertainty in the WNA inputs. Therefore, if $X_{\max} \ll X_{rc}(\omega)$, waves do not propagate close to the resonance cone and all three methods produce diffusion rates that agree within the level of approximation inherent in the model.

If waves propagate very near the resonance cone, which is likely to occur for upper band chorus waves, the effective WNA distribution for method G&H05 becomes highly peaked at the resonance cone (see Figure 3b). This is not satisfactory because upper band chorus waves are observed with a range of WNAs from $\theta \sim 0$ to $\theta \sim \theta_{rc}$ (Li et al., 2016). However, methods H13 and C23 have a similar effective WNA distribution, and the resulting diffusion rates agree within the level of approximation inherent in the model. Since all the diffusion rates used in the BAS-RBM have been calculated using method H13, recalculating all the diffusion rates using method C23 would not produce meaningful differences.

As described in Section 2.1, method G&H05 is very sensitive to the upper integration limit near the resonance cone, and a variety of different approaches have been used in the literature. We have focused on the method originally published in Glauert and Horne (2005), which uses $X_{\max} = \min\left(X_{\max}^{in}, 0.9999 X_{rc}(\omega)\right)$. However, given a different method and a set of input parameters, the effective WNA distribution could be calculated to verify that issues at the resonance cone are properly mitigated.

6. Summary and Conclusions

We have compared three methods to specify the wave spectrum in diffusion rate calculations. The first method was implemented by Glauert and Horne (2005). The second method is a modification that suppresses the magnetic wave power at the cold plasma resonance cone (Horne et al., 2013), and has been used to calculate the entire library of diffusion rates for the BAS Radiation Belt Model. The third method was newly proposed by Cunningham (2023). The methods are referred to as G&H05, H13 and C23 respectively, and the difference between the methods is the distribution of wave energy with respect to wave normal angle (WNA). Observed WNAs are highly variable (Bortnik et al., 2025; Crabtree et al., 2017; Santolík, Kletzing, et al., 2014), and there are inherent uncertainties associated with the assumptions and averaging procedures used to estimate the WNA distribution for quasi-linear diffusion rate calculations. Therefore, the statistical variability of the wave normal angle is likely to be larger than small differences in the angular distribution of wave energy due to the method of calculation. We calculated bounce-averaged pitch angle and energy diffusion rates using typical input parameters for several wave types observed in the inner magnetosphere. The conclusions are summarized below:

1. If waves propagate very close to the resonance cone in method G&H05, the wave energy is highly peaked at the resonance cone, which is not satisfactory. However, this issue is mitigated in methods H13 and C23.
2. Bounce-averaged diffusion rates using methods H13 and C23 consistently agree within a factor of 1.10 for lower band chorus waves, 1.64 for upper band chorus waves, 1.24 for hiss waves and 2.95 for fast magnetosonic waves. These factors are likely much smaller than the uncertainties introduced by statistical averaging of wave data. Note that fast magnetosonic waves do not have a resonance cone and usually have a minor contribution to the overall diffusion rate in global simulations of the radiation belts (Glauert et al., 2024; Meredith et al., 2009).
3. If the resonance cone angle is large compared to the maximum wave normal angle included in the calculation, method G&H05 agrees with the other two methods within the level of approximation inherent in the model. For example, bounce-averaged diffusion rates using methods G&H05 and C23 consistently agree within a factor of 1.09 for lower band chorus waves, 1.05 for hiss waves and 2.76 for fast magnetosonic waves.
4. Method H13, which has been used to calculate the entire library of diffusion matrices used in the BAS-RBM, agrees with method C23 within the level of approximation inherent in the model. This supports the continued use of existing diffusion matrices for modeling and forecasting with the BAS-RBM.

We conclude that uncertainties in modeling global variations in the radiation belts are more likely due to statistical sampling of the data, rather than the method of calculating diffusion rates. However, method C23 offers conceptual and practical advantages which are described in Section 2.1. Therefore, we recommend using method C23 for future work.

Appendix A: Contribution of Individual Harmonic Resonances to the Total Diffusion Rate

Calculating a local quasi-linear diffusion rate involves a sum over integer harmonics n and an integral over $X = \tan\theta$ (the tangent of the wave normal angle). The integrand is evaluated at the resonant frequencies and wavenumbers, which are obtained by simultaneously solving the cold plasma dispersion relation and the resonance condition $\omega - v_{\|}k_{\|} = -n|\Omega_e|/\gamma$ (Albert, 2005; Glauert & Horne, 2005). Therefore, only waves satisfying the resonance condition contribute to the diffusion rate. In this Appendix, we focus on the contribution of individual harmonic resonances to the total diffusion rate, and consider the resonant frequencies and wavenumbers associated with each harmonic. This approach can be helpful to understand why the total bounce-averaged diffusion rates presented in Sections 3 and 4 exhibit very small differences between methods H13 and C23, even though method H13 has more wave power very close to the resonance cone (see Figure 3b). We focus on the upper band chorus calculations, a case where waves propagate close to the resonance cone. The input parameters are described in Section 3.1. We focus on local diffusion rates at the equator, since the resonance cone angle is minimized at the equator and we therefore expect the largest differences. For brevity, we focus on $E = 10$ keV, although similar reasoning can be used to understand the results at higher energies.

Figure A1a shows how different harmonic integers n result in different resonant frequencies and wavenumbers. The whistler mode dispersion relation is shown in black for $\theta = 45°$, and the resonance cone is seen at $\omega = 0.62\Omega_e$ where $k \rightarrow \infty$. The dashed lines show the resonance condition for $\alpha = 45°$, $\theta = 45°$ and several

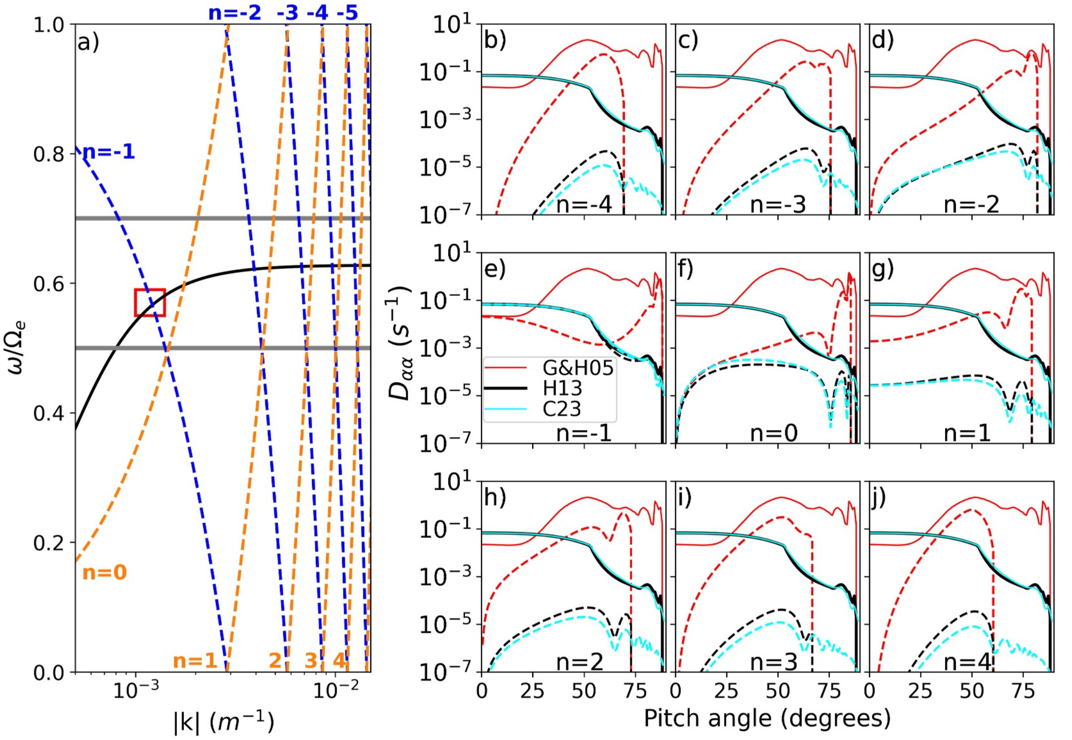

Figure A1. Contribution of individual harmonic resonances to the local pitch angle diffusion rates for upper band chorus waves and $E = 10$ keV electrons. (a) The whistler mode dispersion relation for $\theta = 45°$. The dashed lines show the resonance condition for $\alpha = 45°$ and several values of n; blue indicates $k_{\|} < 0$ and orange indicates $k_{\|} > 0$. The horizontal gray lines are the cutoff frequencies. (b)–(j) The contribution of individual integer harmonics $-4 \leq n \leq 4$ (dashed lines) to the total pitch angle diffusion rate (solid lines). Three different methods are used to specify the wave spectrum: G&H05 (red), H13 (black) and C23 (cyan).

values of n; blue indicates $k_{\|} < 0$ and orange indicates $k_{\|} > 0$. The points where the dispersion relation and resonance condition intersect give the resonant frequency and wavenumber. For example, the intersection of the $n = -1$ resonance with the dispersion relation is highlighted by the red box.

Figures A1b–A1j show the contribution of individual harmonic resonances (dashed lines) to the local pitch angle diffusion rate at the equator (solid lines). Even though the total diffusion rate includes $-10 \leq n \leq 10$, we focus on $-4 \leq n \leq 4$ because the higher order resonances have a smaller contribution to the total diffusion rate. Figure A1e shows that the total diffusion rate in methods H13 and C23 is dominated by the $n = -1$ resonance. It is difficult to discern the dashed black and dashed cyan lines because they overlap with the solid lines. For the $n = -1$ diffusion rate, the differences between methods H13 and C23 are very small for $\alpha < 85°$. This can be understood by considering the resonant frequencies and wavenumbers. The intersection of the $n = -1$ resonance and the dispersion relation occurs away from the resonance cone, which is highlighted by the red box in Figure A1. Since the $n = -1$ resonant frequencies and wavenumbers occur away from the resonance cone, the weighting of wave energy is very similar between methods H13 and C23 (see Figure 3b), which means the resulting diffusion rates exhibit very small differences. The total diffusion rates are very similar between methods H13 and C23 because the $n = -1$ harmonic has the dominant contribution to the total diffusion rate.

It is important to remember that the resonance condition depends on the pitch angle α, and that Figure A1a is plotted for $\alpha = 45°$. Whilst the analysis above applies for $\alpha < 85°$, the $n = -1$ resonant wavenumber increases and approaches the resonance cone as $\alpha \rightarrow 90°$. Therefore, for $\alpha > 85°$ the resonant frequencies and wavenumbers occur close to the resonance cone where method H13 has a higher weighting of wave energy. Close inspection of Figure A1e for $\alpha > 85°$ does reveal larger diffusion rates with method H13 by a factor of ~3 compared with method C23.

Higher order harmonics do produce interactions close to the resonance cone, which is seen in Figure A1a. Since the resonant frequencies and wavenumbers occur close to the resonance cone, the weighting of wave energy in method H13 is greater than for method C23 (see Figure 3b). Therefore, method H13 can produce larger diffusion rates than method C23 by a factor of ~3, for example, in Figure A1b at $\alpha \sim 60°$. However, in methods H13 and C23, these higher order resonances have a small contribution to the total diffusion rate.

Section 3.4 describes how the distribution of wave energy in method G&H05 is highly peaked at the resonance cone. Therefore, higher order harmonics, which produce interactions very close to the resonance cone, have a much more significant contribution in method G&H05. It is clearly seen in Figure A1 that the diffusion rates due to higher order resonances often exceed the diffusion rates due to the $n = -1$ harmonic.

Conflict of Interest

The authors declare no conflicts of interest relevant to this study.

Availability Statement

No observational data was used for this study. The values plotted in the figures can be downloaded at https://doi.org/10.5281/zenodo.19471115 (Sadler, 2026).

Acknowledgments

JDS thanks Gregory S. Cunningham for useful discussions. JDS was supported by a UK Natural Environmental Research Council (NERC) C-CLEAR DTP studentship. RBH was supported by NERC Grant NE/Y006178/1 PRESCIENT. SAG was supported by NERC Grants NE/Z000157/1 and NE/X000389/1. TAD was also supported by NERC Grant NE/Z000157/1. JMA was supported by AFOSR Grant 25RVCOR003. GDZ acknowledges support from STFC via the consolidated Grant to the atomic astrophysics group at DAMTP, University of Cambridge (ST/T000481/1), and the large Grant award to the SAMS project (UKRI 1165).

References

Agapitov, O., Artemyev, A., Krasnoselskikh, V., Khotyaintsev, Y. V., Mourenas, D., Breuillard, H., et al. (2013). Statistics of whistler mode waves in the outer radiation belt: Cluster staff-sa measurements. *Journal of Geophysical Research: Space Physics*, *118*(6), 3407–3420. https://doi.org/10.1002/jgra.50312

Albert, J. M. (2005). Evaluation of quasi-linear diffusion coefficients for whistler mode waves in a plasma with arbitrary density ratio. *Journal of Geophysical Research*, *110*(A3). https://doi.org/10.1029/2004ja010844

Albert, J. M. (2017). Quasi-linear diffusion coefficients for highly oblique whistler mode waves. *Journal of Geophysical Research: Space Physics*, *122*(5), 5339–5354. https://doi.org/10.1002/2017ja024124

Albert, J. M., Meredith, N. P., & Horne, R. B. (2009). Three-dimensional diffusion simulation of outer radiation belt electrons during the 9 October 1990 magnetic storm. *Journal of Geophysical Research*, *114*(A9). https://doi.org/10.1029/2009ja014336

Allison, H. J., Shprits, Y. Y., Zhelavskaya, I. S., Wang, D., & Smirnov, A. G. (2021). Gyroresonant wave-particle interactions with chorus waves during extreme depletions of plasma density in the van Allen radiation belts. *Science Advances*, *7*(5), eabc0380. https://doi.org/10.1126/sciadv.abc0380

Artemyev, A., Agapitov, O., Mourenas, D., Krasnoselskikh, V., Shastun, V., & Mozer, F. (2016). Oblique whistler-mode waves in the earth's inner magnetosphere: Energy distribution, origins, and role in radiation belt dynamics. *Space Science Reviews*, *200*(1–4), 261–355. https://doi.org/10.1007/s11214-016-0252-5

Artemyev, A., Agapitov, O. V., Mourenas, D., Krasnoselskikh, V., & Zelenyi, L. M. (2013). Storm-induced energization of radiation belt electrons: Effect of wave obliquity. *Geophysical Research Letters*, *40*(16), 4138–4143. https://doi.org/10.1002/grl.50837

Baker, D. N., Blake, J. B., Callis, L. B., Cummings, J. R., Hovestadt, D., Kanekal, S., et al. (1994). Relativistic electron acceleration and decay time scales in the inner and outer radiation belts: Sampex. *Geophysical Research Letters*, *21*(6), 409–412. https://doi.org/10.1029/93GL03532

Baker, D. N., Erickson, P. J., Fennell, J. F., Foster, J. C., Jaynes, A. N., & Verronen, P. T. (2017). Space weather effects in the earth's radiation belts. *Space Science Reviews*, *214*(1), 17. https://doi.org/10.1007/s11214-017-0452-7

Bortnik, J., Chen, L., Zhang, X.-J., & Meredith, N. P. (2025). Evolution of dayside chorus into nightside plasmaspheric hiss. *Frontiers in Astronomy and Space Sciences*, *12*, 1619877. https://doi.org/10.3389/fspas.2025.1619877

Crabtree, C., Tejero, E., Ganguli, G., Hospodarsky, G. B., & Kletzing, C. A. (2017). Bayesian spectral analysis of chorus subelements from the van Allen probes. *Journal of Geophysical Research: Space Physics*, *122*(6), 6088–6106. https://doi.org/10.1002/2016JA023547

Cunningham, G. S. (2023). Resolution of a few problems in the application of quasilinear theory to calculating diffusion coefficients in heliophysics. *Journal of Geophysical Research: Space Physics*, *128*(10), e2023JA031703. https://doi.org/10.1029/2023ja031703

Daggitt, T. A., Horne, R. B., Glauert, S. A., & Zanna, G. D. (2024). Reproducing ultra-relativistic electron acceleration using a coupled density and radiation belt model. *Journal of Geophysical Research: Space Physics*, *129*(12), e2024JA032971. https://doi.org/10.1029/2024ja032971

Gao, X., Chen, L., Li, W., Lu, Q., & Wang, S. (2019). Statistical results of the power gap between lower-band and upper-band chorus waves. *Geophysical Research Letters*, *46*(8), 4098–4105. https://doi.org/10.1029/2019GL082140

Glauert, S. A., Atkinson, J. W., Ross, J. P., & Horne, R. B. (2024). A new model of electron pitch angle distributions and loss timescales in the earth's radiation belts. *Journal of Geophysical Research: Space Physics*, *129*(6), e2023JA032249. https://doi.org/10.1029/2023JA032249

Glauert, S. A., & Horne, R. B. (2005). Calculation of pitch angle and energy diffusion coefficients with the padie code. *Journal of Geophysical Research*, *110*(A4). https://doi.org/10.1029/2004ja010851

Glauert, S. A., Horne, R. B., & Meredith, N. P. (2014). 01). Three-dimensional electron radiation belt simulations using the bas radiation belt model with new diffusion models for chorus, plasmaspheric hiss, and lightning-generated whistlers. *Journal of Geophysical Research: Space Physics*, *119*(1), 268–289. https://doi.org/10.1002/2013ja019281

Horne, R. B., Daggitt, T. A., Meredith, N. P., Glauert, S. A., Liu, X., & Chen, L. (2024). Measuring low plasma density in the earth's equatorial magnetosphere from magnetosonic waves. *Geophysical Research Letters*, *51*(12), e2024GL108407. https://doi.org/10.1029/2024gl108407

Horne, R. B., Glauert, S. A., Kirsch, P., Heynderickx, D., Bingham, S., Thorn, P., et al. (2021). The satellite risk prediction and radiation forecast system (sarif). *Space Weather-The International Journal of Research and Applications*, *19*(12), e2021SW002823. https://doi.org/10.1029/2021sw002823

Horne, R. B., Kersten, T., Glauert, S. A., Meredith, N. P., Boscher, D., Sicard-Piet, A., et al. (2013). A new diffusion matrix for whistler mode chorus waves. *Journal of Geophysical Research: Space Physics*, *118*(10), 6302–6318. https://doi.org/10.1002/jgra.50594

Horne, R. B., & Sazhin, S. (1990). Quasielectrostatic and electrostatic approximations for whistler mode waves in the magnetospheric plasma. *Planetary and Space Science*, *38*(2), 311–318. https://doi.org/10.1016/0032-0633(90)90095-8

Horne, R. B., Thorne, R., Glauert, S., Albert, J., Meredith, N., & Anderson, R. (2005). Timescale for radiation belt electron acceleration by whistler mode chorus waves. *Journal of Geophysical Research*, *110*(A3). https://doi.org/10.1029/2004ja010811

Horne, R. B., Thorne, R. M., Glauert, S. A., Meredith, N. P., Pokhotelov, D., & Santolík, O. (2007). Electron acceleration in the van Allen radiation belts by fast magnetosonic waves. *Geophysical Research Letters*, *34*(17). https://doi.org/10.1029/2007gl030267

Horne, R. B., Thorne, R. M., Shprits, Y. Y., Meredith, N. P., Glauert, S. A., Smith, A. J., et al. (2005). Wave acceleration of electrons in the van Allen radiation belts. *Nature*, *437*(7056), 227–230. https://doi.org/10.1038/nature03939

Iucci, N., Levitin, A. E., Belov, A. V., Eroshenko, E. A., Ptitsyna, N. G., Villoresi, G., et al. (2005). Space weather conditions and spacecraft anomalies in different orbits. *Space Weather*, *3*(1). https://doi.org/10.1029/2003SW000056

Jordanova, V., Morley, S., Engel, M., Godinez, H., Yakymenko, K., Henderson, M., et al. (2023). The ram-scb model and its applications to advance space weather forecasting. *Advances in Space Research*, *72*(12), 5596–5606. https://doi.org/10.1016/j.asr.2022.08.077

Kennel, C. F., & Engelmann, F. (1966). Velocity space diffusion from weak plasma turbulence in a magnetic field. *Physics of Fluids*, *9*(12), 2377–2388. https://doi.org/10.1063/1.1761629

Kersten, T., Horne, R. B., Glauert, S. A., Meredith, N. P., Fraser, B. J., & Grew, R. S. (2014). Electron losses from the radiation belts caused by emic waves. *Journal of Geophysical Research: Space Physics*, *119*(11), 8820–8837. https://doi.org/10.1002/2014JA020366

Kletzing, C. A., Bortnik, J., Hospodarsky, G. B., Kŭrth, W. S., Santolik, O., Smitth, C. W., et al. (2023). The electric and magnetic fields instrument suite and integrated science (emfisis): Science, data, and usage best practices. *Space Science Reviews*, *219*(4), 28. https://doi.org/10.1007/s11214-023-00973-z

Lerche, I. (1968). Quasilinear theory of resonant diffusion in a magneto-active, relativistic plasma. *The Physics of Fluids*, *11*(8), 1720–1727. https://doi.org/10.1063/1.1692186

Li, W., Bortnik, J., Thorne, R. M., Cully, C., Chen, L. Q., Angelopoulos, V., et al. (2013). Characteristics of the poynting flux and wave normal vectors of whistler-mode waves observed on themis. *Journal of Geophysical Research: Space Physics*, *118*(4), 1461–1471. https://doi.org/10.1002/jgra.50176

Li, W., & Hudson, M. (2019). Earth's van Allen radiation belts: From discovery to the van Allen probes era. *Journal of Geophysical Research: Space Physics*, *124*(11), 8319–8351. https://doi.org/10.1029/2018JA025940

Li, W., Mourenas, D., Artemyev, A. V., Agapitov, O. V., Bortnik, J., Albert, J. M., et al. (2014). Evidence of stronger pitch angle scattering loss caused by oblique whistler-mode waves as compared with quasi-parallel waves. *Geophysical Research Letters*, *41*(17), 6063–6070. https://doi.org/10.1002/2014gl061260

Li, W., Santolík, O., Bortnik, J., Thorne, R. M., Kletzing, C. A., Kurth, W. S., & Hospodarsky, G. B. (2016). New chorus wave properties near the equator from van Allen probes wave observations. *Geophysical Research Letters*, *43*(10), 4725–4735. https://doi.org/10.1002/2016GL068780

Lyons, L. R. (1974). Pitch angle and energy diffusion coefficients from resonant interactions with ion–cyclotron and whistler waves. *Journal of Plasma Physics*, *12*(3), 417–432. https://doi.org/10.1017/s002237780002537x

Lyons, L. R., & Thorne, R. M. (1973). Equilibrium structure of radiation belt electrons. *Journal of Geophysical Research*, *78*(13), 2142–2149. https://doi.org/10.1029/ja078i013p02142

Lyons, L. R., & Thorne, R. M. (1972). Parasitic pitch angle diffusion of radiation belt particles by ion cyclotron waves. *Journal of Geophysical Research (1896-1977)*, *77*(28), 5608–5616. https://doi.org/10.1029/JA077i028p05608

Lyons, L. R., Thorne, R. M., & Kennel, C. F. (1971). Electron pitch-angle diffusion driven by oblique whistler-mode turbulence. *Journal of Plasma Physics*, *6*(3), 589–606. https://doi.org/10.1017/s0022377800006310

Lyons, L. R., Thorne, R. M., & Kennel, C. F. (1972). Pitch-angle diffusion of radiation belt electrons within the plasmasphere. *Journal of Geophysical Research*, *77*(19), 3455–3474. https://doi.org/10.1029/ja077i019p03455

Lyons, L. R., & Williams, D. J. (1984). *Quantitative aspects of magnetospheric physics*. Springer. https://doi.org/10.1007/978-94-017-2819-5

Lyu, X., Jordanova, V. K., Engel, M., Tu, W., & Ma, Q. (2024). Quantifying the role of emic wave scattering during the 27 February 2014 storm by ram-scb simulations. *Journal of Geophysical Research: Space Physics*, *129*(7), e2024JA032606. https://doi.org/10.1029/2024JA032606

Ma, Q., Artemyev, A. V., Mourenas, D., Li, W., Thorne, R. M., Kletzing, C. A., et al. (2017). Very oblique whistler mode propagation in the radiation belts: Effects of hot plasma and Landau damping. *Geophysical Research Letters*, *44*(24), 12057–12066. https://doi.org/10.1002/2017GL075892

Meredith, N. P., Horne, R. B., Glauert, S. A., Baker, D. N., Kanekal, S. G., & Albert, J. M. (2009). Relativistic electron loss timescales in the slot region. *Journal of Geophysical Research*, *114*(A3). https://doi.org/10.1029/2008ja013889

Meredith, N. P., Horne, R. B., Kersten, T., Li, W., Bortnik, J., Sicard, A., & Yearby, K. H. (2018). Global model of plasmaspheric hiss from multiple satellite observations. *Journal of Geophysical Research: Space Physics*, *123*(6), 4526–4541. https://doi.org/10.1029/2018ja025226

Meredith, N. P., Thorne, R. M., Horne, R. B., Summers, D., Fraser, B. J., & Anderson, R. R. (2003). Statistical analysis of relativistic electron energies for cyclotron resonance with emic waves observed on crres. *Journal of Geophysical Research*, *108*(A6). https://doi.org/10.1029/2002JA009700

Mourenas, D., Artemyev, A. V., Agapitov, O. V., & Krasnoselskikh, V. (2014). Consequences of geomagnetic activity on energization and loss of radiation belt electrons by oblique chorus waves. *Journal of Geophysical Research: Space Physics*, *119*(4), 2775–2796. https://doi.org/10.1002/2013ja019674

Mourenas, D., Artemyev, A. V., Ripoll, J.-F., Agapitov, O. V., & Krasnoselskikh, V. V. (2012). Timescales for electron quasi-linear diffusion by parallel and oblique lower-band chorus waves. *Journal of Geophysical Research*, *117*(A6). https://doi.org/10.1029/2012JA017717

Ni, B., Bortnik, J., Thorne, R. M., Ma, Q., & Chen, L. (2013). Resonant scattering and resultant pitch angle evolution of relativistic electrons by plasmaspheric hiss. *Journal of Geophysical Research: Space Physics*, *118*, 7740–7751. https://doi.org/10.1002/2013ja019260

Ross, J. P. J., Glauert, S. A., Horne, R. B., Watt, C. E., Meredith, N. P., & Woodfield, E. E. (2020). A new approach to constructing models of electron diffusion by emic waves in the radiation belts. *Geophysical Research Letters*, *47*(20), e2020GL088976. https://doi.org/10.1029/2020gl088976

Ross, J. P. J., Glauert, S. A., Horne, R. B., Watt, J., & Meredith, N. P. (2021). On the variability of emic waves and the consequences for the relativistic electron radiation belt population. *Journal of Geophysical Research: Space Physics*, *126*(12), e2021JA029754. https://doi.org/10.1029/2021ja029754

Ross, J. P. J., Meredith, N. P., Glauert, S. A., Horne, R. B., & Clilverd, M. A. (2019). Effects of vlf transmitter waves on the inner belt and slot region. *Journal of Geophysical Research: Space Physics*, *124*(7), 5260–5277. https://doi.org/10.1029/2019JA026716

Sadler, J. D. (2026). Figure data (Version 2.0) [Dataset]. *Zenodo*. https://doi.org/10.5281/ZENODO.19471115

Santolík, O., Kletzing, C. A., Kurth, W. S., Hospodarsky, G. B., & Bounds, S. R. (2014). Fine structure of large-amplitude chorus wave packets. *Geophysical Research Letters*, *41*(2), 293–299. https://doi.org/10.1002/2013GL058889

Santolík, O., Macúšová, E., Kolmašová, I., Cornilleau-Wehrlin, N., & Conchy, Y. d. (2014). Propagation of lower-band whistler-mode waves in the outer van Allen belt: Systematic analysis of 11-years of multi-component data from the cluster spacecraft. *Geophysical Research Letters*, *41*(8), 2729–2737. https://doi.org/10.1002/2014gl059815

Santolík, O., Němec, F., Gereová, K., Macúšová, E., de Conchy, Y., & Cornilleau-Wehrlin, N. (2004). Systematic analysis of equatorial noise below the lower hybrid frequency. *Annales Geophysicae*, *22*(7), 2587–2595. https://doi.org/10.5194/angeo-22-2587-2004

Santolík, O., Parrot, M., & Lefeuvre, F. (2003). Singular value decomposition methods for wave propagation analysis. *Radio Science*, *38*(1). https://doi.org/10.1029/2000rs002523

Selesnick, R. S., Albert, J. M., & Starks, M. J. (2013). Influence of a ground-based vlf radio transmitter on the inner electron radiation belt. *Journal of Geophysical Research: Space Physics*, *118*(2), 628–635. https://doi.org/10.1002/jgra.50095

Shi, R., Mourenas, D., Artemyev, A., Li, W., & Ma, Q. (2018). Highly oblique lower-band chorus statistics: Dependencies of wave power on refractive index and geomagnetic activity. *Journal of Geophysical Research: Space Physics*, *123*(6), 4767–4784. https://doi.org/10.1029/2018JA025337

Shprits, Y. Y., Kellerman, A. C., Drozdov, A. Y., Spence, H. E., Reeves, G. D., & Baker, D. N. (2015). Combined convective and diffusive simulations: Verb-4d comparison with 17 March 2013 van Allen probes observations. *Geophysical Research Letters*, *42*(22), 9600–9608. https://doi.org/10.1002/2015GL065230

Shprits, Y. Y., & Ni, B. (2009). Dependence of the quasi-linear scattering rates on the wave normal distribution of chorus waves. *Journal of Geophysical Research*, *114*(A11). https://doi.org/10.1029/2009JA014223

Stix, T. H. (1992). *Waves in plasmas*. American Institute of Physics.

Storey, L. R. O., & Lefeuvre, F. (1979). The analysis of 6-component measurements of a random electromagnetic wave field in a magnetoplasma – I. The direct problem. *Geophysical Journal International*, *56*(2), 255–269. https://doi.org/10.1111/j.1365-246x.1979.tb00163.x

Subbotin, D. A., & Shprits, Y. Y. (2009). Three-dimensional modeling of the radiation belts using the versatile electron radiation belt (verb) code. *Space Weather*, *7*(10). https://doi.org/10.1029/2008sw000452

Thorne, R. M. (2010). Radiation belt dynamics: The importance of wave-particle interactions. *Geophysical Research Letters*, *37*(22). https://doi.org/10.1029/2010GL044990

Thorne, R. M., Li, W., Ni, B., Ma, Q., Bortnik, J., Chen, L., et al. (2013). Rapid local acceleration of relativistic radiation-belt electrons by magnetospheric chorus. *Nature*, *504*(7480), 411–414. https://doi.org/10.1038/nature12889

Thorne, R. M., Ni, B., Tao, X., Horne, R. B., & Meredith, N. P. (2010). Scattering by chorus waves as the dominant cause of diffuse auroral precipitation. *Nature*, *467*(7318), 943–946. https://doi.org/10.1038/nature09467

Tu, W., Cunningham, G. S., Chen, Y., Morley, S. K., Reeves, G. D., Blake, J. B., et al. (2014). Event-specific chorus wave and electron seed population models in dream3d using the van Allen probes. *Geophysical Research Letters*, *41*(5), 1359–1366. https://doi.org/10.1002/2013gl058819

Varotsou, A., Boscher, D., Bourdarie, S., Horne, R. B., Glauert, S. A., & Meredith, N. P. (2005). Simulation of the outer radiation belt electrons near geosynchronous orbit including both radial diffusion and resonant interaction with whistler-mode chorus waves. *Geophysical Research Letters*, *32*(19). https://doi.org/10.1029/2005gl023282

Wong, J., Meredith, N. P., Horne, R. B., Glauert, S. A., & Ross, J. P. J. (2022). Electron diffusion by magnetosonic waves in the earth's radiation belts. *Journal of Geophysical Research: Space Physics*, *127*(4), e2021JA030196. https://doi.org/10.1029/2021JA030196

Wong, J., Meredith, N. P., Horne, R. B., Glauert, S. A., & Ross, J. P. J. (2023). New chorus diffusion coefficients for radiation belt modeling. *Journal of Geophysical Research: Space Physics*, *129*(1), e2023JA031607. https://doi.org/10.1029/2023ja031607

Wrenn, G. L. (1995). Conclusive evidence for internal dielectric charging anomalies on geosynchronous communications spacecraft. *Journal of Spacecraft and Rockets*, *32*(3), 514–520. https://doi.org/10.2514/3.26645